Geophys. J. R. astr. Soc. (1982) **68**, 389–427

Mantle convection as a boundary layer phenomenon

Gary T. Jarvis* and W. R. Peltier *Department of Physics, University of Toronto, Toronto, Ontario M5S 1A7, Canada*

Received 1981 May 19; in original form 1981 February 19

Summary. The boundary layer nature of vigorous thermal convection is explored using high resolution numerical solutions to the governing hydrodynamic equations. These solutions are obtained for a series of idealized models of the Earth's mantle in which the viscosity is assumed to be constant. A detailed analysis of the local energy balance within the horizontal and vertical thermal boundary layers is presented in terms of which a test of the fundamental assumptions of boundary layer theory is provided. The results of this test have important geophysical consequences since the asymptotic predictions of boundary layer theory have been employed extensively in the context of thermal history modelling. Although boundary layer theory closely predicts the correct power-law behaviour of various quantities it does not determine their absolute values accurately. Vertical advection is shown to play an important role in the energy balance within horizontal boundary layers at all Rayleigh numbers. Horizontal and vertical advection dominate the energy balance within vertical plumes while horizontal diffusion plays a very minor role. When heating is partially from within the fluid, vertical advection into the upper thermal boundary layer can produce significant departures in the thermal structure from that found when heating is entirely from below. For a free upper boundary this results in a relative flattening of the variations of surface topography and heat flow across the convection cells. For a constant velocity upper boundary (similar to plate motion) the bathymetry flattens but the heat flow does not; this result agrees with marine observations. Rigidity of the thermal boundary layer below the upper surface is not included explicitly in the model, and it is not known whether the inclusion of this feature in future models would significantly alter the topographic expression. If not, the observed departure of the oceanic bathymetry from a $\sqrt{\text{age}}$ dependence at old ocean floor ages could be attributed to a small amount of internal heating in a mantle-wide convective circulation.

*Present address: Department of Geology, University of Toronto, Toronto, Ontario M5S 1A1, Canada.

1 Introduction

Convection in the Earth's mantle is a high Rayleigh number phenomenon. Consequently temperature variations within the flow are concentrated in narrow horizontal and vertical boundary layers which surround adiabatic interior regions. Since virtually all of the heat transfer in vigorous convection is effected through these boundary layers a detailed analysis of their thermal structure will lead to a better understanding of heat transport within the mantle.

The need for such an analysis is indicated by recent developments both in boundary layer theories of mantle convection and in the modelling of planetary thermal histories. In both of these areas particularly simple aspects of vigorous convection are exploited in order to generate approximate results which can then be applied to more complex geophysical problems while avoiding the additional complexities of the non-linear hydrodynamic equations themselves. In the former, the fact that temperature variations are concentrated within the boundary layers is utilized to predict the actual temperature structure (Roberts 1979; Olson & Corcos 1980). In the latter, simple (semi-empirically derived) power-law relationships between the Rayleigh number and various quantities of interest are used to parameterize the influence of mantle convection upon the internal energy budget of the interior (Tozer 1967, 1972, 1974; McKenzie & Weiss 1975; Sharpe & Peltier 1978, 1979; Cassen *et al.* 1979; Kaula 1979; Schubert, Cassen & Young 1979; Turcotte, Cooke & Willeman 1979; Daly 1980; Davies 1980). Both of these simplifying aspects of vigorous convection are a consequence of the boundary layer behaviour at high Rayleigh number and our main purpose in this paper is to provide a detailed and quantitative description of this behaviour.

There are two approaches which one might take in producing such an analysis: (a) that embodied in boundary layer theory, and (b) direct numerical integration of the governing field equations. The major advantage of the former approach is its simplicity, in that computations of the temperature field are confined to the region of interest while ignoring the nearly adiabatic core of the convection cell. The disadvantage, however, is that due to the necessary additional simplifying assumptions, boundary layer theory delivers only approximate answers to the questions of interest. Furthermore, boundary layer theory cannot be applied when the convective circulation is even partly forced by heating from within. This is a severe restriction in the context of the geophysical problem since we expect that the Earth's mantle must experience at least some internal heating due to radioactivity and this will contribute to the forcing of the circulation. In order to address the geophysically relevant issues we are therefore obliged to resort to direct numerical integration of the governing equations.

Because of the high Rayleigh number of mantle convection, the thermal boundary layers are thin and a major portion of the numerical integration is involved in obtaining the nearly adiabatic passive flow field in the central core of the cells. In order to achieve adequate numerical resolution of the boundary layers we have used relatively fine finite-difference meshes with a maximum of 96×96 intervals. This has resulted in sufficient detail within the boundary layers to enable direct comparison with the thermal structure predicted by boundary layer theory. Converged steady-state solutions were obtained for a range of Rayleigh numbers encompassing those believed to be appropriate to the Earth's mantle. Therefore, subject to certain assumptions, the numerical results may be related directly to the geophysical problem. In this paper we examine the validity of these assumptions and, subject to the restrictions which they impose, explore the implications of our calculations for convection in the Earth's mantle.

In Section 2 we briefly review the physical and mathematical structure of the convection problem, focusing on the special case of this general problem which is most relevant to the

planetary interior. Section 3 concerns a detailed discussion of the boundary layer nature of the numerical solutions and in it we obtain an estimate of the value of the Rayleigh number above which boundary layer behaviour is first fully revealed. This section also includes a detailed assessment of the validity of boundary layer theory for heated from below convection in which we particularly stress the importance of the vertical advection of heat in the local energy balance within the horizontal boundary layers. Section 3 ends with a discussion of the effects of internal heat generation on the thermal structure of the upper boundary layer and we demonstrate that these effects are primarily a consequence of vertical advection. Section 4 is devoted to the application of our numerical results to the problem of convection in the Earth's mantle and to an assessment of the difficulties which such application entails. In particular the variation of the heat flow and equilibrium topography across the upper surface of typical convection cells is related to various geophysical models of mantle convection. Our conclusions are summarized in Section 5.

2 Mathematical formulation of the convection problem

The field equations of classical hydrodynamics are expressions for the pointwise conservation of mass, momentum, and energy which are completed by a suitable thermodynamic equation of state. For incompressible fluids, these have the respective forms (e.g. Landau & Lifshitz 1959):

$$\nabla \cdot \mathbf{u} = 0, \tag{1}$$

$$\rho\left(\frac{\partial \mathbf{u}}{\partial t} + \mathbf{u} \cdot \nabla \mathbf{u}\right) = -\nabla p + \rho \mathbf{g} + \nabla \cdot \tau \tag{2}$$

$$\rho C_{\mathrm{p}}\left(\frac{\partial T}{\partial t} + \mathbf{u} \cdot \nabla T\right) = \nabla \cdot (K \nabla T) + H, \tag{3}$$

$$\rho = \rho_{\mathrm{d}}[1 - \alpha(T - T_{\mathrm{d}})]; \tag{4}$$

in which $\mathbf{u}$ and ρ are the velocity and density fields, t is time, p is the pressure field, g the assumed constant gravitational acceleration, τ the deviatoric stress tensor, C_{p} the specific heat at constant pressure, T the absolute temperature, K the thermal conductivity, and H the rate of heating per unit volume. In the equation of state (4), which has been assumed linear and in which the isothermal compressibility has been neglected, the parameter $\rho_{\mathrm{d}} = \rho(T = T_{\mathrm{d}})$ where T_{d} is a reference temperature, and α is the coefficient of thermal expansion. If the stress–strain relation is Newtonian and the fluid is incompressible and isotropic, then

$$\tau_{ij} = \eta\left(\frac{\partial u_i}{\partial x_j} + \frac{\partial u_j}{\partial x_i}\right) \tag{5}$$

where η is the dynamic viscosity. In the Earth the diffusivities of momentum and heat are such that the Prandtl number $Pr = \eta C_{\mathrm{p}}/K$ is essentially infinite, in which case the inertial force on the left side of (2) is completely negligible.

Throughout this paper we shall be concerned with a model of convection in a horizontal layer of fixed depth d subject to free-slip (zero tangential stress) conditions on both upper and lower boundaries. The corresponding boundary conditions on the temperature field will be formulated in such a way that we may move smoothly from models which are heated from below to models which are heated from within. For this reason the condition at the upper surface will always be one of constant temperature while at the lower boundary we shall impose either a condition of constant temperature or a condition of constant heat flux.

All of the solutions we shall discuss will pertain to square boxes (i.e. unit aspect ratio cells), the vertical boundaries of which are planes of mirror symmetry with respect to the temperature and velocity fields. The numerical scheme employed is essentially the same as that in McKenzie, Roberts & Weiss (1974) and Jarvis & McKenzie (1980) except that, for finite-difference grids consisting of other than 24 x 24 or 48 x 48 mesh points, we have used a new direct solver for the Poisson equation (Swarztrauber & Sweet 1975) which is more flexible (though less efficient).

For convenience of presentation, all of the hydrodynamic fields have been non-dimensionalized through introduction of the characteristic scales

$$(x, z) = d(x', z'); \qquad T = T_1 T' + T_d; \qquad t = \frac{d}{U} t'$$

$$\mathbf{u} = U\mathbf{u}'; \qquad U = \frac{g\alpha T_1 d^2}{\nu}; \qquad \rho = \rho_d \rho'; \qquad P = \rho_d g d P' \tag{6}$$

where x is the horizontal coordinate, z is the vertical coordinate $[0, d]$ measured positively upwards, the primed variables are dimensionless, T_d is the (constant) temperature of the upper surface, ν is the kinematic viscosity (η/ρ), and the characteristic temperature T_1 depends upon the thermal boundary condition to be applied at the lower surface ($z = 0$). If we impose a constant temperature T_0 at $z = 0$ then $T_1 = \Delta T = (T_0 - T_d)$, whereas if we hold the heat flux fixed then T_0 is undetermined and we arbitrarily choose $T_1 = 1°C$. Substitution of (6) into (1)–(5) yields the system

$$\nabla \cdot \mathbf{u} = 0 \tag{7}$$

$$-\nabla p = -\rho \hat{k} + \alpha T_1 \nabla^2 \mathbf{u} \tag{8}$$

$$\frac{DT}{Dt} = \kappa' \nabla^2 T + \epsilon' \tag{9}$$

where the primes have been dropped. In (7)–(9) $\hat{k}$ is a unit vector in the positive z-direction, and κ' and ϵ' are the dimensionless thermal diffusivity and heating rate given by

$$\kappa' = \frac{K\nu}{g\alpha T_1 d^3 \rho_d C_p} \tag{10a}$$

$$\epsilon' = \frac{H\nu}{g\alpha T_1^2 d \rho_d C_p}. \tag{10b}$$

Here we shall be concerned only with two-dimensional flows confined to the $x-z$ plane and can therefore satisfy the solenoidal condition (7) by defining $\mathbf{u}$ in terms of a stream function Ψ such that $\mathbf{u} = (-\partial\Psi/\partial z, 0, \partial\Psi/\partial x)$. The pressure field may be eliminated by taking the curl of (8) which yields

$$\nabla^2 \omega = \frac{\partial T}{\partial x} \tag{11}$$

where ω is the y-component of the dimensionless vorticity $\boldsymbol{\omega}$ defined by

$$\boldsymbol{\omega} = \nabla \times \mathbf{u}. \tag{12}$$

Substituting in (12) for $\mathbf{u}$ in terms of Ψ yields

$$\nabla^2 \Psi = -\omega. \tag{13}$$

Equations (9), (11), and (13) determine the time-dependent temperature and velocity fields and contain two dimensionless parameters κ' and ϵ'. Two alternate and more useful

parameters can be constructed from these which are μ, the ratio of internal heat production to the total heat flow across the upper surface of the box, and R, the Rayleigh number. If F is the heat flux into the base of the box then

$$\mu = \frac{Hd}{F + Hd}. \tag{14}$$

For a constant temperature lower boundary condition and $\mu = 0$ (the so-called Bénard configuration; Bénard 1901) the (Bénard) Rayleigh number is defined as (Jeffreys 1926)

$$R_B = \frac{g\alpha \Delta T d^3}{\kappa \nu} \tag{15}$$

while for the case of constant heat flux through the lower boundary and $\mu \geq 0$ (as investigated by Roberts 1967) the (Roberts) Rayleigh number is

$$R_R = \frac{g\alpha d^4 (F + Hd)}{\rho_d C_p \kappa^2 \nu} \tag{16}$$

where $\kappa = K/\rho_d C_p$ is the dimensional thermal diffusivity. Note that for Bénard convection $\kappa' = R_B^{-1}$.

2.1 APPLICATION TO THE EARTH

Although the above field equations were derived for incompressible fluids, we wish to apply them to the Earth's mantle across which the density increases by 60–70 per cent. Jeffreys (1930) showed that the equations for the *onset* of convection (i.e. infinitesimal motion) were the same for compressible fluids as for incompressible fluids if the temperature gradient in excess of the local adiabatic gradient was employed in place of the actual gradient, but only if the overall variations of density and of the adiabatic gradient are small. Even this equivalence breaks down at finite flow velocities because of the greater relative importance in compressible fluids of the non-linear terms representing the frictional dissipation of kinetic energy into heat (ignored for infinitesimal motions). Jeffreys' conclusion has nevertheless been widely quoted as authority for the use of Boussinesq's (1903) incompressible approximation in studies of mantle convection. Spiegel & Veronis (1960), Mihaljan (1962), and Malkus (1964) have subsequently demonstrated through scale analysis that this approximation is justified for finite amplitude convection only when the length scale over which the density varies significantly is much greater than the depth over which convection itself extends. For the Earth's mantle this condition requires

$$\frac{d}{H_T} \ll 1 \tag{17}$$

where $H_T = C_p/g\alpha$ is the adiabatic temperature scale height of the mantle (Peltier 1972; Hewitt, McKenzie & Weiss 1975).

For mantle convection Jarvis & McKenzie (1980) estimate values of $d/H_T \simeq 0.3$ for convection confined to the upper mantle (0–700 km depth) and $d/H_T \simeq 0.6$ for the whole mantle (0–2900 km). Thus, particularly for the whole mantle, equation (17) is not rigorously satisfied and hence use of the Boussinesq approximation cannot be justified by scale analysis. However, numerical solutions of the non-linear equations governing the temperature and velocity fields in a compressible fluid (Jarvis & McKenzie 1980) do appear to provide the required justification. These calculations show that for $d/H_T = 0.5$, the main influence of compressibility and viscous dissipation combined is that due to the variation of the adiabatic gradient. Thus, assuming that the adiabatic gradient in the mantle is reasonably

Table 1. Physical parameters for whole mantle models.

$g = 10\ \mathrm{m\ s^{-1}}$	
$\alpha = 1.4 \times 10^{-5}\ \mathrm{K^{-1}}$	
$\rho_d = 4.9 \times 10^3\ \mathrm{kg\ m^{-3}}$	$(4.9\ \mathrm{g\ cm^{-3}})$
$d = 2.9 \times 10^3\ \mathrm{km}$	
$\eta = 4.9 \times 10^{21}\ \mathrm{kg\ m^{-1}\ s^{-1}}$	$(4.9 \times 10^{22}\ \mathrm{P})$
$\kappa = 2.5 \times 10^{-6}\ \mathrm{m^2\ s^{-1}}$	$(2.5 \times 10^{-2}\ \mathrm{cm^2\ s^{-1}})$
$C_p = 1.2 \times 10^3\ \mathrm{J\ kg^{-1}\ K^{-1}}$	
$\nu = 1.0 \times 10^{18}\ \mathrm{m^2\ s^{-1}}$	$(1.0 \times 10^{22}\ \mathrm{cm^2\ s^{-1}})$

constant the properties of the circulation should be well represented by solutions of the Boussinesq equations (7)–(9). In application of these solutions to the Earth it must then be understood that the values of ΔT and F in (14), (15) and (16) must be interpreted as values in excess of those associated with a constant adiabatic gradient.

The Rayleigh number appropriate to convection in the Earth's mantle depends strongly upon the depth of the convecting zone. Unfortunately the depth extent of the circulation involving plate creation and destruction is a matter of current debate. The two main hypotheses are: (a) that convection is confined to the upper 700 km of the mantle (e.g. Turcotte & Oxburgh 1967, 1972; Richter 1973a; McKenzie *et al.* 1974; McKenzie & Weiss 1975; Parmentier & Turcotte 1978; Richter & McKenzie 1978), and (b) that convection extends throughout the mantle from the Earth's surface to the core–mantle boundary (e.g. Hess 1962; Peltier 1972; Davies 1977; O'Connell 1977; Sharpe & Peltier 1978, 1979; Elsasser, Olson & Marsh 1979; Peltier 1980). Geophysical and geochemical data are not yet sufficiently discriminating, of themselves, to rule out completely either hypothesis and the analysis presented here reflects this impasse. We do not argue in favour of either hypothesis, but rather consider the implications of scaling simple numerical models to each case.

For the case of upper mantle convection we shall employ the same values for the physical parameters as those adopted by McKenzie *et al.* (1974) which lead to $R_R = 1.4 \times 10^6$ or $R_B = 1.2 \times 10^5$ (see equation 21). For the case of whole mantle convection we may employ the values listed in Table 1 as representative. Allowing for the spherical geometry of the Earth we estimate a mean heat flow at mid-mantle depth of about 94 mW m^{-2}, based on an oceanic heat flow of 58 mW m^{-2}. A mean mantle viscosity of $\eta = 5 \times 10^{22}$ poise is consistent with post-glacial rebound analyses which indicate an upper mantle viscosity of 10^{22} poise (Peltier, Farrell & Clark 1978; Peltier 1981) increasing to values of approximately 10^{23} poise through the seismic discontintuity at 670 km depth (Wu & Peltier, in preparation). With these values we estimate $R_R = 2.5 \times 10^7$ for the whole mantle. There is considerable uncertainty in this estimate, however, since heat flow in particular has likely been underestimated. A separate estimate of R_B may be obtained by assuming $\Delta T = 3000°C$ in excess of adiabatic, which yields $R_B \approx 4 \times 10^6 \approx 5 \times 10^3\ R_c$ where R_c is the critical Rayleigh number (equation 19). The numerical solutions discussed in the following section encompass the above range of estimates of R_R and R_B.

3 Numerical solutions

The finite difference calculations discussed here all pertain to steady state single cell solutions with aspect ratio (width : depth) equal to one. We shall initially consider models with no internal heating ($\mu = 0$) for which the lower boundary is held at constant temperature. For this heating configuration the Nusselt number Nu is the ratio of the actual heat flow across the layer to that which would be effected in the absence of convection, or

$$Nu = \left(\frac{d}{\Delta T}\right)\left(\frac{d\langle T\rangle}{dz}\bigg|_{z=d}\right) \tag{18}$$

where $\langle\rangle$ represents the horizontal average. For $R_B \leqslant R_c$ (where R_c is the critical Rayleigh number for the onset of convection), $Nu = 1$; for $R_B > R_c$, $Nu > 1$. With the free-slip, constant temperature boundary conditions employed in this case R_c can be obtained analytically as

$$R_c = [\pi^2 + (\pi/a)^2]^3 (a/\pi)^2 \tag{19}$$

where a is the aspect ratio (Chandrasekhar 1961). For $a = 1$, the case with which we are concerned, $R_c = 779.273$.

Subsequent to our discussion of solutions to the Bénard problem we shall consider models with a constant heat flux lower boundary condition and $0 \leqslant \mu \leqslant 1$. For such models the heat flux across the layer is the same regardless of whether or not convection occurs while the temperature drop ΔT becomes a free parameter. In terms of this free parameter we may define a new Nusselt number as

$$Nu' = \frac{\Delta T_{cond}}{\Delta T} \tag{20}$$

where ΔT is the actual temperature difference across the layer and ΔT_{cond} is that which would exist in the absence of convection. As for the Bénard problem, there is a critical Rayleigh number R_c' such that for $R_R \leqslant R_c'$, $Nu' = 1$ while for $R_R > R_c'$, $Nu' > 1$. The value of R_c' must be determined numerically in this case and for $\mu = 0$ with an aspect ratio of one it is $R_c' = 586.8$ (Jarvis & McKenzie 1980). Comparing solutions with constant heat flux and constant temperature lower boundary conditions (with $\mu = 0$), McKenzie *et al.* (1974) found that $Nu' \approx Nu$ when

$$R_R = 0.231 R_B^{4/3}. \tag{21}$$

From this it follows that the Rayleigh number appropriate to mantle convection expressed in terms of one boundary condition may differ from that in terms of the other by more than an order of magnitude when the Nusselt numbers are equal. It is therefore important to keep clearly in mind which Rayleigh number is relevant in a given context.

Our discussion of the numerical results will commence with those for the Bénard configuration since boundary layer theory for this case is reasonably well developed. There is also a numerical advantage gained in this case because the mean temperature is known in advance as $T_d + \Delta T/2$ and this increases the rate of convergence to the steady state.

3.1 THE BOUNDARY LAYER NATURE OF HIGH RAYLEIGH NUMBER FLOWS

In Fig. 1 we compare streamlines, isotherms, and vertical profiles of horizontally averaged temperature and horizontal velocity at Rayleigh numbers $R_B = 10R_c$ and $R_B = 10^4 R_c$. Although R_B differs by three orders of magnitude in the two cases, the Ψ contours and horizontal velocity profiles reveal only small qualitative differences. The isotherm contours and mean temperature profiles, however, are radically different. At low R_B the cold isotherms are advected downwards and the hot isotherms upwards, resulting in the generation of a gravitationally stable central zone as indicated by the reversal of the vertical gradient of the mean temperature profile. At high R_B the isotherms are swept clear of the central zone into thin boundary layers which surround the cell. The corresponding mean temperature profile clearly shows the steep gradients in the upper and lower thermal boundary layers and the isothermal nature of the central core. The mean profile of the horizontal component of velocity u, on the other hand, reveals no similar boundary layer structure. Due to the high value of the Prandtl number, inertial effects are unimportant and velocity boundary layers cannot develop in such a viscously dominated flow. The profile has the form of a simple

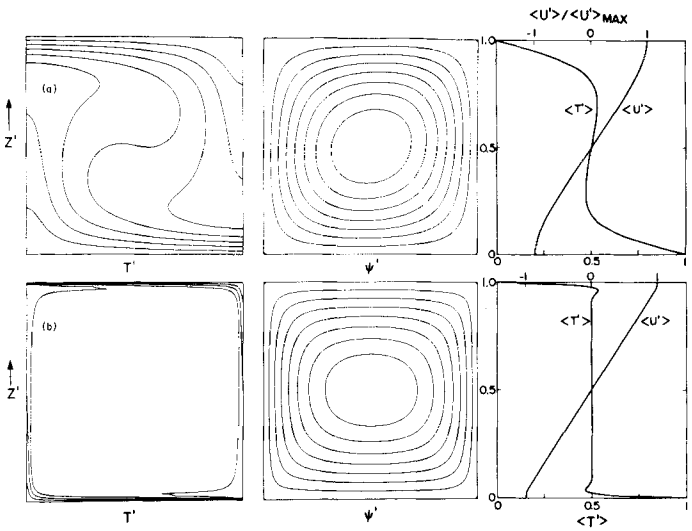

Figure 1. Contours of dimensionless temperature T' and streamfunction Ψ' and vertical profiles of horizontally averaged temperature $\langle T' \rangle$ and horizontal component of velocity $\langle u' \rangle$. (The symbol $\langle\ \rangle$ indicates the horizontal average of the enclosed quantity.) The scale for $\langle T' \rangle$ is indicated at the bottom of each graph while that for $\langle u' \rangle$ (expressed as a fraction of the maximum value $\langle u' \rangle_{max}$) is indicated at the top of each graph. (a) $R_B = 10R_c$; steady-state solution obtained on a 24×24 finite-difference grid. Contours: T', 0 (1/8), 1; Ψ', 0 (2.25×10^{-4}) 1.95×10^{-3}; $\langle u' \rangle_{max} = 4.42 \times 10^{-3}$. (b) $R_B = 10^4 R_c$; steady-state solution obtained on a 96×96 finite-difference grid. Contours: T', 0 (1/7) 1, Ψ', 0 (1.88×10^{-5}) 1.50×10^{-4}; $\langle u' \rangle_{max} = 4.16 \times 10^{-4}$. Dimensional values are obtained by multiplying T' and $\langle T' \rangle$ by ΔT (obtained from R_B and equation (15)), Ψ' by κR_B and $\langle u' \rangle$ by $\kappa R_B/d$. The circulation is clockwise in both solutions.

shear flow through the thermal boundary layers and isothermal core alike with the only edge effect being due to the mechanical free-slip condition ($\partial u/\partial z = 0$) on the upper and lower horizontal boundaries.

Fig. 2 illustrates the transition of the mean temperature field into the boundary layer dominated form in more detail as R_B is increased from R_c to $10^4 R_c$. Initially, as R_B increases, the mean temperature profile acquires a reversed temperature gradient which con-

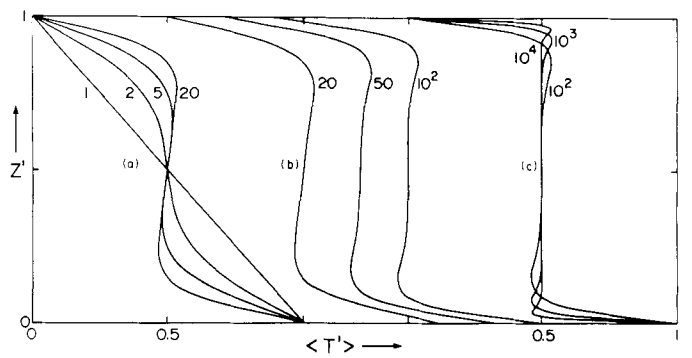

Figure 2. Vertical profiles of horizontally averaged dimensionless temperature $\langle T' \rangle$ for several values of R_B. Each profile is labelled with the corresponding value of R_B/R_c. (a) Low Rayleigh number regime. (b) Transition to boundary layer regime. (c) Boundary layer regime. Steady-state solutions obtained on the following grids: 24×24 for $R_B \leqslant 20\ R_c$; 48×48 for $R_B = 50\ R_c$; 80×80 for $R_B = 10^2 R_c$ and $5 \times 10^2 R_c$; 96×96 for $R_B > 5 \times 10^2 R_c$.

tinues to increase until $R_B \approx 20\,R_c$ (Fig. 2a). For $R_B \gtrsim 50\,R_c$ the central zone of reversed temperature gradient is split by an isothermal region (Fig. 2b), the extent of which increases with R_B. As the volume occupied by the isothermal region increases, the regions of steepest negative temperature gradient and the adjacent regions in which the gradient is reversed are forced closer to the horizontal boundaries (Fig. 2c). Gradients in the central zone are actually positive (reversed) but are substantially smaller than those associated with the horizontal thermal boundary layers – for $R_B \geqslant 500\,R_c$ by two or more orders of magnitude. This weak central gradient in the mean field reflects the broadening of the hot and cold plumes as they move vertically and does not imply the existence of a positive temperature gradient in the core of the two-dimensional cell as we shall see. Values of R_B representative of upper mantle and whole mantle convection ($150\,R_c$ and $5 \times 10^3 R_c$, respectively, see above) both lie well within the regime of Rayleigh numbers for which the thermal boundary layers are well developed.

The overshoot of the boundary layer temperature profiles beyond the mean temperature in the cell core is due to horizontal advection out of the plumes near the stagnation points while the boundary layer thickness is determined by the pinching effect of transverse advection in the same regions. These processes are illustrated in Fig. 3 where we show a series of local vertical and horizontal temperature profiles through a cell at $R_B = 10^3 R_c$. The vertical temperature profile on the left of Fig. 3(a) through the centre of the hot plume shows that as hot material is swept upwards its temperature decreases little until it approaches very close to the upper boundary. The depth of the thermal boundary layer is least above the rising hot plume and is governed primarily by a balance between the heat conducted down the steep temperature gradient and that advected upwards in the plume. The rising plume material has higher than average temperatures and as it moves horizontally below the constant temperature upper boundary it loses heat through diffusion, both through the upper surface and into the underlying central core, thus accounting for the region for reversed temperature gradient immediately above the isothermal core. The diffusive cooling of the top boundary layer as it moves horizontally leads to an increase of its thickness as it

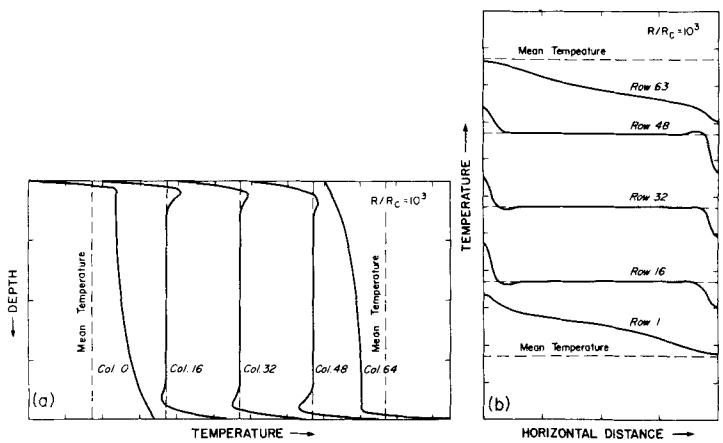

Figure 3. Vertical and horizontal profiles of dimensionless temperature across a convection cell for which $R_B = 10^3 R_c$ obtained on a 64×64 finite-difference grid. (a) Vertical profiles along columns of the numerical grid as indicated. Column 0 corresponds to the centre of the rising plume (at the left of the box), while Column 64 corresponds to the centre of the descending plume (at the right of the box). The broken vertical lines indicate the mean temperature of the box of fluid. (b) Horizontal profiles along rows of the numerical grid as indicated. Row 1 is one grid-plane above the (constant temperature) bottom of the box. Row 63 is one grid-plane below the (constant temperature) top of the box. The broken horizontal lines indicate the mean temperature of the box of fluid.

moves towards the stagnation point above the cold descending plume. In Fig. 3(b) the horizontal temperature profiles reveal the narrow hot rising plume at the left and the cold sinking plume at the right. The rise in temperature adjacent to the sinking plume and the dip in temperature next to the rising plume are due respectively to the entrainment of hot material from the rising plume by the cold sinking jet and of cold material from the sinking jet by the hot plume. This is a peculiar characteristic of steady flow, which arises because of the diffusive broadening of the boundary layers.

In Fig. 4 we have overlaid the vertical and horizontal profiles in a square domain with the isothermal portion of each profile positioned at the coordinate along which the profile was taken. This presentation is similar to that obtained from the isotherm contours but reveals more precisely the local forms of both the boundary layers and plumes. A single isotherm for $T = \Delta T/2$ is shown superimposed upon Fig. 4(a) to illustrate the geometric connection of the various boundary layers. Fig. 4(b) shows the sensitivity of the boundary layer structure when R_B is increased by an order of magnitude to $R_B = 10^4 R_c$; the boundary layer thickness decreases by approximately a factor of 2. The solution shown in Fig. 4(b) was obtained at the limits of numerical resolution on the 96 x 96 mesh since the number of grid points across the boundary layer ranges from as few as 2 to as many as 6. Fortunately, Rayleigh numbers relevant to mantle convection are probably not larger than this (see above) and finer meshes may not be required.

The most fundamental prediction of boundary layer theory, in so far as the modelling of planetary thermal history is concerned is the dependence of the heat transfer upon the Rayleigh number. For sufficiently large values of R_B the prediction is that

$$Nu = c(a)\,[R_B/R_c]^{1/3} \tag{22}$$

where $c(a)$ is a constant of proportionality whose value depends upon the aspect ratio a. Plotting Nu, determined from our numerical solutions, against R_B/R_c (Fig. 5) we find that a power-law relationship is obeyed at large R_B, with an exponent of 0.313. This agrees with boundary layer theory (blt) to within 6 per cent. At sufficiently small values of R_B, the Nusselt number is less than the blt prediction by an amount which decreases with increasing R_B. The transition into the power-law regime occurs at $R_B \approx 50 R_c$, which is the minimum Rayleigh number noted previously for which the mean temperature field adopts its characteristic boundary layer form (see Fig. 2b). This is in accord with the power-law behaviour of the boundary layer thickness δ, and mean velocities, $\bar{u}$ and $\bar{w}$, at the horizontal and vertical boundaries of the cell, which are also plotted in Fig. 5.

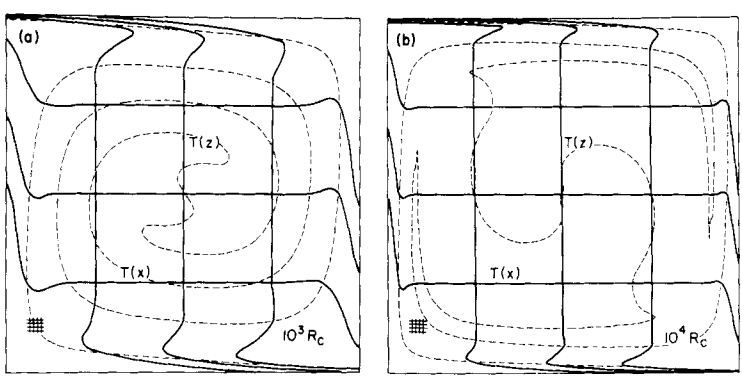

Figure 4. Superimposed vertical and horizontal temperature profiles (solid curves) and a single isotherm at $\Delta T/2$ (dashed curve), the mean temperature of the box. The isothermal segment of each profile is positioned along the coordinate for which the profile is plotted. Steady solutions shown in (a) $R_B = 10^3 R_c$ and (b) for $R_B = 10^4 R_c$ were both obtained on 96 x 96 finite-difference grids.

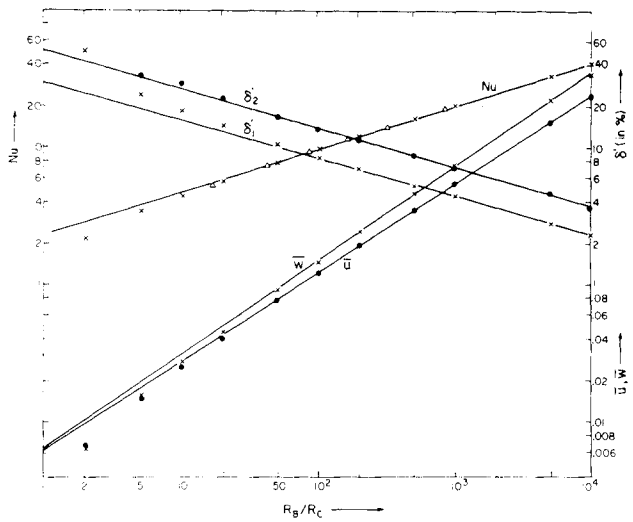

Figure 5. Nusset number Nu, dimensionless boundary layer thickness δ', mean (dimensionless) horizontal velocity at upper surface $\bar{u}$, and mean (dimensionless) vertical velocity in centre of rising plume $\bar{w}$, all plotted against the ratio R_B/R_c. All variables are plotted on logarithmic scales so that linear trends indicate power-law dependence on R_B/R_c. Points indicated by solid circles (•) or x's (×) at different values of R_B/R_c correspond to different numerical solutions. The straight lines are the least-squares best fits to points in the range $R_B/R_c \geqslant 10^2$. The lines labelled δ_1' and δ_2' refer to the boundary layer thickness defined by the depth at which the mean temperature $(T_d + \Delta T/2)$ is first reached, and the depth of the peak overshoot of temperature above the mean, respectively. Slopes of the straight lines are: Nu, 0.313; δ_1', −0.278; δ_2', −0.285; $\bar{u}$, 0.645; $\bar{w}$, 0.684. The triangles plotted along the Nu curve indicate values of Nu computed by Moore & Weiss (1973). Velocities may be re-dimensionalized by multiplying by 3.71 cm yr^{-1} for a whole mantle circulation or by 9.24 cm yr^{-1} for an upper mantle circulation.

For $R_B/R_c \geqslant 50$, the upper and lower boundary layers are isolated by the isothermal core of the convection cell and do not interact. Fig. 2(c) shows that in this range the similarity of the temperature profiles is striking and extends to the amount by which the boundary layer temperatures overshoot that in the cell interior. A formal demonstration of this feature is given by Richter & McKenzie (1981) who have shown that mean temperature profiles (in the boundary layer regime) may be closely approximated by the sum of two power series involving appropriately scaled depths, the Rayleigh number and coefficients which are *independent* of the Rayleigh number. The following simple scaling argument provides a physical understanding of this behaviour. Since $R_B \propto d^3$ and $Nu \propto R_B^{1/3}$ (approximately) an increase in d by a factor of f produces an increase in R_B by a factor of f^3 and in Nu by f. From (18) this implies that the near surface temperature gradient remains constant, so that the temperature profile over the new depth is produced by simply adding an isothermal segment of length $d(f-1)$ to the central zone. When re-plotted on a dimensionless height scale from 0 to 1 the effect is as shown in Fig. 2(c) with the boundary layer thickness δ varying approximately as $R_B^{-1/3}$. Fig. 6 illustrates the result of applying this procedure to the profile for $R_B = 50\,R_c$. Figs 6(b) and 6(c) illustrate good agreement between the synthetic profiles obtained geometrically through this scaling argument and those computed exactly for $R_B = 10^3 R_c$ and $R_B = 10^4 R_c$ respectively. The small discrepancy between synthetic and computed profiles is due to the fact that the power-law dependence of the boundary layer thickness δ on R_B/R_c (deduced from the data plotted in Fig. 5) is only −0.28 rather than that anticipated by the simple scaling argument above of −0.33. Consequently, although the synthetic and computed profiles for $R_B/R_c = 10^2$ (not shown) are indistinguishable, as we

move further from the reference case ($50R_c$) the synthetic boundary layers thin more rapidly with R_B than those of the exact solutions. Although the synthetic profiles were produced by varying d and re-scaling depth they can be scaled back to dimensional profiles with any new values of d and ΔT provided R_B is unchanged. This feature of the temperature profiles for high Rayleigh number convection has an important application in thermal history modelling since the detailed profiles obtained from numerical calculations could be simulated within a parameterization scheme such as that employed by Sharpe & Peltier (1979).

The success of boundary layer theory in closely predicting the correct power law dependence of Nu upon R_B/R_c is well demonstrated by Figs 5 and 6. Recent blt analyses by Roberts (1979) and Olson & Corcos (1980) can also account for the overshoot of the boundary layer temperature profile beyond the temperature of the isothermal core. However, blt does not appear to determine the constants of proportionality very accurately. Roberts (1979) compared his predictions of $c(a)$ from blt with values derived from the Galerkin analysis of Straus (1972) and from the finite-difference solutions of Moore & Weiss (1973). Roberts' values disagree with the numerically derived values by 40 per cent at $a = 1$ and show a much stronger dependence upon a than that obtained from the exact numerical solutions. In this connection it should be noted that mean values of $c(a = 1)$ obtained by the two different numerical models agree to within 1 per cent of one another, with a range of less than 4 per cent among the individual estimates. It would therefore appear that the Nusselt number, and hence the temperatures within the boundary layer, cannot be accurately determined by boundary layer theory alone. Since this limitation may be a consequence of some error in the initial assumptions of blt we will proceed to directly assess the validity of these assumptions by checking them against the numerical solutions. In particular we shall examine the nature of the local energy balance within the upper thermal boundary layer. This analysis will prove to be of particular interest when we attempt to apply the model solutions to the Earth's mantle.

Such a study will only be meaningful, however, if our model solutions closely approximate the true solutions and consequently we shall first examine the reliability of our numerical computations.

3.2 ACCURACY OF THE NUMERICAL SOLUTIONS

The accuracy of stable solutions to the difference equations, which are consistent with the original differential equations, is governed by the rate at which these solutions converge to

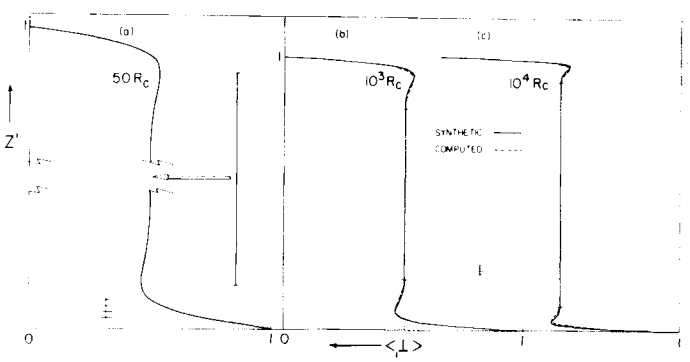

Figure 6. Construction of synthetic temperature profiles. (a) An isothermal segment of length $d(f-1)$ is spliced into the centre of a reference profile at $R_B = 50R_c$. The resulting profile corresponds to that for $R_B = 50f^3R_c$. Examples of synthetic profiles (——), rescaled to a dimensionless height of 1, are compared with computed model profiles (----) for (b) $R_B = 10^3R_c$, i.e. $f^3 = 20$, and (c) $R_B = 10^4R_c$, i.e. $f^3 = 200$.

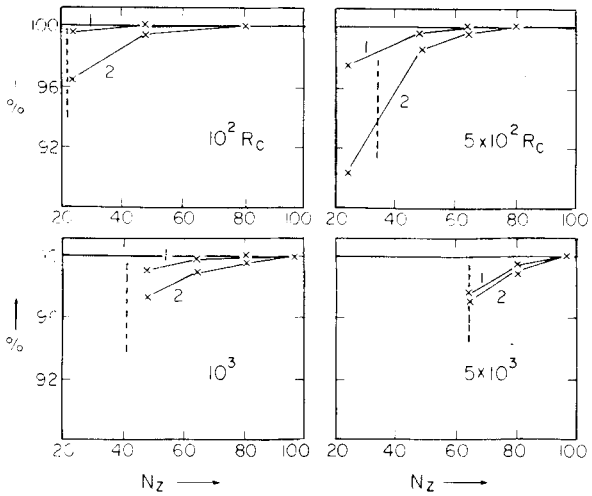

Figure 7. Convergence of the numerical solutions. Ψ_{max} (curve 1) and Nu (curve 2), expressed as a percentage of their respective values at highest resolution, plotted against N_z the number of intervals across the numerical grid (in either direction). Examples are shown for four different values of R_B as indicated at the lower right of each graph. The vertical dashed line on each graph indicates the minimum number of intervals considered acceptable by the criterion, suggested by Moore & Weiss (1973), that at least three intervals span each boundary layer.

constant values as the spacing of the numerical grid is reduced. Since the velocity field is much smoother than the temperature field we can expect convergence to be more rapid for, say, the maximum value of Ψ, Ψ_{max}, than for the Nusselt number. Fig. 7 illustrates the convergence of these two parameters, for several models, as the number of intervals N_z across the grid (in each direction) is increased. Because values in the limit $N_z \to \infty$ are unknown, individual values have been plotted as a percentage of those obtained at highest resolution. The upper curve (labelled 1) in each graph represents the convergence of Ψ_{max} while the lower curve (2) represents that of Nu. Thus, the accuracy of the computed heat transport would be greatly over-estimated if based upon percentage changes of Ψ_{max} from one grid spacing to the next. Since we are concerned with heat transport within the boundary layers an appropriate measure of convergence is provided by the lower curve in these graphs.

For comparative purposes the vertical dashed lines indicate the number of intervals required (at each Rayleigh number) to satisfy the condition imposed by Moore & Weiss (1973) that at least three intervals span each boundary layer. Fig. 7 illustrates that this condition roughly corresponds to an accuracy of 2 per cent in Ψ_{max} and 5 per cent in Nu. As our solutions have all been obtained on considerably finer meshes we expect that these figures will be at least halved in most cases.

A final point worth noting here is that constancy of the Nusselt number as a function of height (in a model solution) does not imply convergence although it does indicate steady-state conditions. For example, for steady solutions with $R_B = 10^2 R_c$ and $R_B = 10^3 R_c$, at lowest resolution the Nusselt number was constant with height to within 0.04 per cent and 0.05 per cent respectively although the actual values were less than those at highest resolution by 4 and 3 per cent respectively.

3.3 LOCAL ENERGY BALANCE WITHIN THE HORIZONTAL BOUNDARY LAYERS

A basic assumption made in most boundary layer theories of convection is that the horizontal velocity u is a constant function of x (the horizontal coordinate) within the hori-

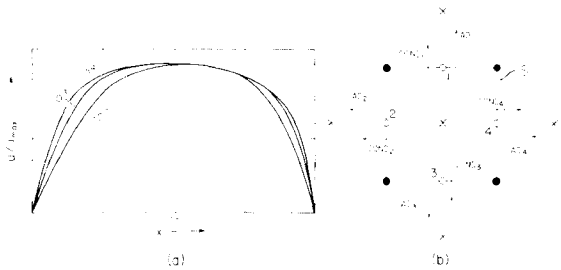

Figure 8. (a) Horizontal velocity u' at the upper surface of model convection cells for various values of R_B/R_c (as labelled) expressed as a ratio of their respective maximum values u'_{max} (b) A small portion of the finite-difference grid indicating the volume element bounded by the surface S. Grid points are indicated by circles and x's. The four faces of S are individually labelled as 1, 2, 3 and 4. Conductive fluxes across each face are computed in terms of temperature at the grid points labelled X. Advective fluxes are computed in terms of temperature at the points labelled with open circles and streamfunction at the points labelled with solid circles. $COND_i$ is the conducted flux across the ith face; AD_i is the advected flux across the ith face.

zontal boundary layers. In Fig. 8(a) $u(x)$ at the upper surface is plotted as a function of R_B/R_c. Relatively constant velocities, at high Rayleigh numbers, are confined to a central zone covering about 50 per cent of the cell. Although the extent of this zone increases with R_B, the dependence is very weak. Since the maximum value of R_B/R_c appropriate to mantle convection is less than 10^4, plate-like surface motions (i.e. $\partial u/\partial x = 0$) could not be produced in a constant viscosity mantle.

The importance of $\partial u/\partial x \neq 0$ can be appreciated by considering the steady-state temperature equation. In the absence of internal heat sources

$$u\frac{\partial T}{\partial x} + w\frac{\partial T}{\partial z} = \kappa\frac{\partial^2 T}{\partial x^2} + \kappa\frac{\partial^2 T}{\partial z^2}, \tag{23}$$

where u and w are the horizontal and vertical components of the velocity vector $\mathbf{u}$. At the upper surface $w = 0$, and from continuity (equation 1) $\partial w/\partial z = -\partial u/\partial x$; hence if $\partial u/\partial x = 0$ in the boundary layer, then $w = 0$ and the second term in (23), which represents the rate of temperature change due to vertical advection, vanishes. With the additional assumption that $\partial^2 T/\partial x^2 \ll \partial^2 T/\partial z^2$ in horizontal boundary layers, the equation governing heat transfer in the thermal boundary layer becomes

$$u\frac{\partial T}{\partial x} = \kappa\frac{\partial^2 T}{\partial z^2}. \tag{24}$$

However, when $\partial u/\partial x \neq 0$, $w \neq 0$ and although $u \gg w$ we have $\partial T/\partial x \ll \partial T/\partial z$ and, therefore, it is not clear that ignoring vertical advection is justified. Nevertheless, at high Rayleigh numbers we can expect vertical advection to be unimportant in the central zone where $\partial u/\partial x \approx 0$.

To examine the relative importance of conduction and advection in the horizontal and vertical directions we integrate equation (23) over a volume δv with square cross-section of dimension $2h$ (where h is the mesh spacing of the finite-difference grid) centred on a grid-point within the thermal boundary layer (Fig. 8b). This yields

$$\int_{\delta v} \mathbf{u}\cdot\nabla T\, dv = \int_{\delta v} \kappa\nabla^2 T\, dv \tag{25}$$

or

$$\oint_S T\mathbf{u}\cdot\mathbf{n}\, dS = \oint_S \kappa\nabla T\cdot\mathbf{n}\, dS \tag{26}$$

where **n** is a unit outward pointing normal to the bounding surface S. Here we have made use of the continuity equation to equate $\mathbf{u}\cdot\nabla\mathbf{T}$ with $\nabla\cdot T\mathbf{u}$ and then applied Gauss' theorem to both sides of (25). If we label the top, left, bottom and right faces of the surface S as 1, 2, 3, and 4 respectively, the equation (26) can be approximated as

$$2h\sum_{i=1}^{4}(AD_i + COND_i) = 0 \tag{27}$$

where the subscript i indicates a quantity at the mid-point of the ith face of S and $AD_i = (\mathbf{u}\cdot\mathbf{n})_i T_i$ is the advected, and $COND_i = -\kappa(\nabla T\cdot\mathbf{n})_i$ the conducted, flux of temperature outwards across the ith face (see Fig. 8b).

In Figs 9(a) and (b) we have plotted the horizontal variations of the eight individual flux components appearing in equation (27), evaluated along a row of volume elements centred one grid-plane below the upper surface, for a high Rayleigh number flow. Since face 1 of S is, in this case, the upper surface of the convection cell, for each volume element $AD_1 = 0$ and

$$COND_1 = -\sum_{i=2}^{4}(AD_i + COND_i). \tag{28}$$

The horizontal advective fluxes (AD_2 and AD_4) have the largest magnitudes at all x, but are of opposite sign. Vertical advection (AD_3) is most important near the plumes. The hori-

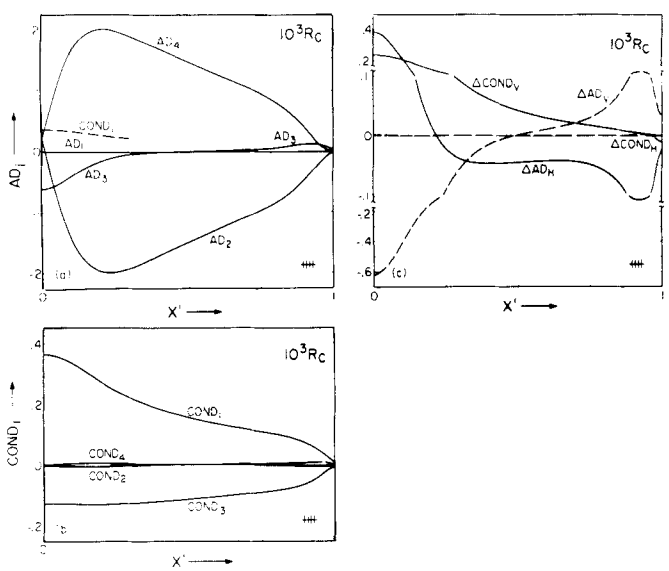

Figure 9. Contributions of the flux components to the local energy balance plotted as a function of (dimensionless) horizontal distance x' within the upper thermal boundary layer, for $R_B = 10^3 R_C$. These graphs correspond to a depth one grid-plane below the upper surface. Solution obtained on a 96×96 finite difference grid. (a) Dimensionless advective fluxes AD_i, $i = 1, 2, 3, 4$, across the four faces of S (see text and Fig. 8b). (b) Dimensionless conductive fluxes $COND_i$, $i = 1, 2, 3, 4$ across the four faces of S. (c) Net horizontal and vertical, advective and conductive, fluxes outwards across S. $\Delta AD_H = AD_2 + AD_4$, $\Delta AD_V = AD_1 + AD_3$, $\Delta COND_H = COND_2 + COND_4$, $\Delta COND_V = COND_1 + COND_3$. Ordinate scales indicate the relative magnitudes of the various flux components. Dimensional units may be obtained by multiplying by $cR_B K\Delta T/d$, where $c = 3.072\times10^{-6}$.

zontal conductive fluxes ($COND_2$ and $COND_4$) are negligible compared to vertical conductive fluxes, but comparable to each other and of opposite sign. Since the energy balance is determined by the sum of the flux components, in Fig. 9(c) we have plotted

$$\begin{aligned} \Delta AD_{\mathrm{H}} &= AD_2 + AD_4 \\ \Delta AD_{\mathrm{V}} &= AD_1 + AD_3 \\ \Delta COND_{\mathrm{H}} &= COND_2 + COND_4 \\ \Delta COND_{\mathrm{V}} &= COND_1 + COND_3, \end{aligned} \tag{29}$$

where ΔAD_{H} is the net flux out of the volume element due to horizontal advection, ΔAD_{V} is the net outward flux due to vertical advection, and so forth. Away from the plumes it is generally assumed that horizontal advection balances vertical diffusion or, in our notation, that

$$\Delta AD_{\mathrm{H}} = -\Delta COND_{\mathrm{V}} \tag{30}$$

and that ΔAD_{V} and $\Delta COND_{\mathrm{H}}$ are negligible. Fig. 9(c) confirms that $\Delta COND_{\mathrm{H}} \approx 0$. However, throughout much of the central zone vertical advection (ΔAD_{V}) is comparable to or greater than vertical conduction. Except in the near vicinity of the mid-point of the cell, where $w \approx 0$, the correct energetic balance is

$$\Delta AD_{\mathrm{H}} + \Delta AD_{\mathrm{V}} = -\Delta COND_{\mathrm{V}}. \tag{31}$$

Close to the mid-point of the convection cell, where horizontal velocity gradients are small, the temperature on face 2 of S is higher than that on face 4 and horizontal advection produces a net influx of heat ($\Delta AD_{\mathrm{H}} < 0$). This influx is balanced primarily by a net vertical conductive out-flow across S ($\Delta COND_{\mathrm{V}} > 0$). To the left of centre the magnitude of ΔAD_{H} is reduced because the horizontal velocity on face 2 of S is less than that on face 4. However, vertical advection in this region supplements the influx of heat across S by an amount which is greater than the decrease in $|\Delta AD_{\mathrm{H}}|$ (see Fig. 9c). Further left, in spite of larger horizontal temperature gradients, horizontal velocity gradients become sufficiently steep that horizontal advection produces a net outflow of heat ($\Delta AD_{\mathrm{H}} > 0$). Above the upwelling plume, vertical advection produces a relatively large net influx of heat which is balanced by a net vertical conductive and horizontal advective flux out of each volume element. To the right of centre horizontal velocity gradients are negative which tends to offset the effects of a diminishing horizontal temperature gradient. Thus, horizontal advection produces a greater influx of heat than predicted by boundary layer theory, but this is more than compensated for by a net outflow due to vertical advection ($\Delta AD_{\mathrm{V}} > 0$). Close to the sinking plume vertical diffusion becomes negligible ($\Delta COND_{\mathrm{V}} \to 0$) and the balance is primarily between vertical and horizontal advection. (Above the centre of the sinking plume *horizontal* diffusion, although small, becomes comparable to the advective fluxes.) The overall effect at the surface is to produce a surface heat flow which is greater than that predicted by boundary layer theory to the left of centre and less than predicted to the right. However, since the thermal effects of $\partial u/\partial x \neq 0$ and $w \neq 0$ contribute in opposite senses, the departure from boundary layer predictions is not large at high Rayleigh numbers (see Fig. 12 for example).

This discussion has concerned the energy balance one grid-plane below the surface at $R_{\mathrm{B}} = 10^3 R_{\mathrm{c}}$. Fig. 10 shows plots similar to Fig. 9(c) for $R_{\mathrm{B}} = 10^2 R_{\mathrm{c}}$ and $R_{\mathrm{B}} = 10^4 R_{\mathrm{c}}$. The main qualitative difference between these graphs is that the influence of the plumes recedes substantially towards the edges at high Rayleigh numbers. Nevertheless, vertical advection remains comparable to the other terms in the local energy balance, except near the mid-point of the cell, at all Rayleigh numbers.

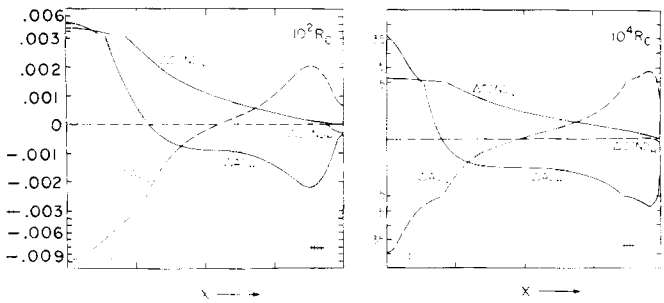

Figure 10. Same as Fig. 9(c) but for (a) $R_B = 10^2 R_c$ and (b) $R_B = 10^4 R_c$. Dimensional units are obtained by multiplying by $cR_B K \Delta T/d$ where $c = 3.072 \times 10^{-4}$ for (a), and $c = 3.072 \times 10^{-8}$ for (b). The scaling used here allows direct comparison of relative magnitudes for Figs 9–11 if the same physical parameters are assumed for all cases.

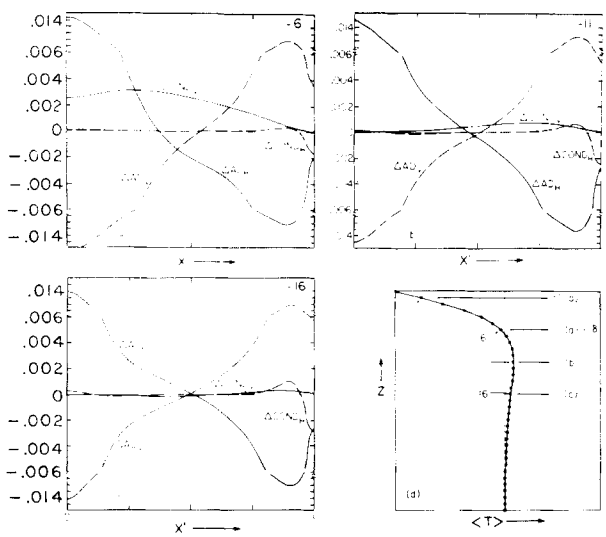

Figure 11. Same as Fig. 10(a) except for depths of: (a) six grid-planes below the upper surface, (b) 11 grid-planes below the upper surface, and (c) 16 grid-planes below the upper surface. The depths of these planes relative to the mean temperature variation and boundary layer thickness δ (same as δ_2 in Fig. 5) are shown in (d). Each grid plane is indicated by a solid circle. Depths corresponding to Figs 10(a), 11(a–c) are also indicated.

The changing character of the energy balance with depth is shown in Figs 11(a)–(c) for a model with $R_B/R_c = 10^2$. Fig. 11(d) indicates the relative depths in the thermal boundary layer corresponding to Figs 11(a)–(c) which are plotted for depths 6, 11 and 16 grid-planes below the upper surface. In the upper portion of the boundary layer (Fig. 11a) the general character of the energy balance remains similar to that at the surface, except that the edge effects of the plumes migrate inwards. This is due to the increase in vertical velocity with depth within the thermal boundary layer. At a depth centred on the peak of the mean temperature profile through the boundary layer (Fig. 11b) vertical diffusion plays a minor role in the local balance, and horizontal advection does not produce a net influx of heat until close to the mid-point of the cell. Below the depth of peak temperatures (Fig. 11c) the balance is primarily between horizontal and vertical advection. From a Lagrangian frame of

reference (moving with a fluid parcel) this implies that the temperature of the fluid is not changing as it moves through this portion of the grid. (In fact, a slight diffusive warming does occur ($\Delta COND_V < 0$) in the central region due to the curvature of the temperature profile.)

3.4 SURFACE HEAT FLOW

In their initial boundary layer theory of mantle convection, Turcotte & Oxburgh (1967) only considered the major temperature drop across the boundary layer and ignored the overshoot of the temperature profile beyond the mean value of the central core. This theory predicts surface heat flow $F_u \alpha x^{-1/2}$. Figs 11(b) and (c) show that the departure of the actual temperature profile from that used by Turcotte & Oxburgh should have little influence on their result. Vertical advection within the boundary layer, however, could be expected to influence this result. In Fig. 12(a) we have plotted the surface heat flow F_u, computed at the upper surface of a convection model with $R_B = 5 \times 10^3 R_c$ and compared this with a curve proportional to $x^{-1/2}$ and constrained to fit the computed curve at the point indicated by the small arrow. The surface heat flow was computed by identifying F_u with $COND_1$ in equation (28) and evaluating (28) over a box of dimension h centred one-half a grid-plane below the upper surface, interpolating T and Ψ where necessary. A Rayleigh number $R_B = 5 \times 10^3 R_c$ corresponds to our estimate of the maximum value appropriate to convection in the Earth's mantle (see discussion above). As anticipated from the discussion of Fig. 9(c) the computed heat flow falls below the reference curve to the right of centre and above to the left. The discrepancy to the left of centre is reduced by the fact that the reference curve approaches infinity as $x \to 0$, whereas the computed flux remains finite, thus necessi-

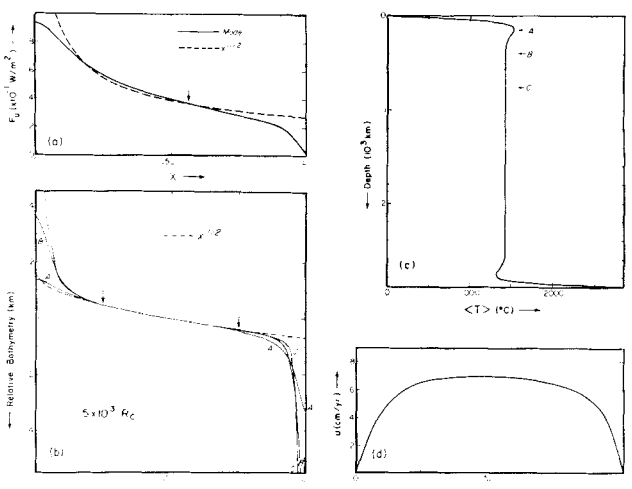

Figure 12. Model predictions for $R_B = 5 \times 10^3 R_c$ dimensionalized using the physical parameters listed in Table 1. (a) Variation of surface heat flux across the upper surface of the convection cell (——) compared to a reference curve proportional to $x^{-1/2}$ (----) which is constrained to have the same value as the model prediction at the point indicated by the small arrow. L is the horizontal dimension of the cell. (b) Bathymetric variation across the top of the convection cell, measured in km relative to the mid-point L/2. The three curves labelled A, B and C result from equation (32) when compensation is assumed to occur at the depths indicated in (c) as A, B, C respectively. The dashed curve varies linearly with $x^{1/2}$ and is constrained to fit curve B at the points indicated by the small arrows. (c) Mean vertical temperature profile. Depths A, B and C indicate values of z_1 (equation 32) used in (b). (d) Variation of horizontal surface velocity across the top of the convection cell.

tating a second cross-over. Away from the edges, the overall trend of the computed curve does not deviate substantially from an $x^{-1/2}$ behaviour. Thus boundary layer theory provides a reasonable prediction of the power-law dependence of F_u on x, particularly to the left of centre.

3.5 SURFACE TOPOGRAPHY

Integrating the temperature structure in the thermal boundary layer and assuming isostatic compensation below, boundary layer theory predicts that the surface topography should vary as $x^{1/2}$. If we assume the upper surface of the convection cell to be overlain with sea-water, the increase in the water depth $D(x)$, relative to that at $x = 0$, is predicted to be

$$D_1(x) = \frac{\alpha \rho_m}{\rho_m - \rho_w} \int_0^{z_1} [T(0, z^*) - T(x, z^*)]\, dz^* \tag{32}$$

(Oxburgh & Turcotte 1978), where ρ_m is the mean mantle density, ρ_w is the density of sea-water, z^* is the depth measured downwards and z_1 is the assumed depth of isostatic compensation. Using equation (32), we have computed $D(x)$ from the numerical model with $R_B = 5 \times 10^3 R_c$. The resulting bathymetry profiles shown in Fig. 12(b) are for three different values of z_1. The solid curves labelled A, B, and C result when compensation is assumed to occur at the depths indicated in Fig. 12(c) by the arrows labelled A, B, and C respectively. When plotted relative to the depth at the mid-point the three curves overlie each other in the central region suggesting that compensation has occurred by depth A, the base of the thermal boundary layer. The dashed line in Fig. 12(b) varies linearly with $x^{1/2}$ and is constrained to fit curve B at the points indicated by the two arrows. Away from the edges the agreement is quite satisfactory.

The expression for $D_1(x)$ given by (32) breaks down close to the edges of the box due to the explicit assumption of isostasy and the implicit assumption in the derivation of (32) that $T(0, z^*) \approx T(x, z^*)$ for $z^* > z_1$ (below the thermal boundary layer) for all x; at all depths in the hot rising plume $T > T_c$, the temperature of the isothermal central core of the convection cell, and in the cold sinking plume $T < T_c$. Hence, the deeper we choose z_1 the greater the computed density deficit above the rising plume and the greater the density excess above the sinking plume. Nevertheless, by depth A, just below the stagnation point of the rising plume, the accumulated density deficit is not sufficient to cause significant departure from the reference $x^{1/2}$ curve. Therefore, whenever equation (32) is used we will take z_1 to be at the base of the thermal boundary layer.

Application of equation (32) is restricted to high Rayleigh number convection cells for which the boundary layer approximations can be justified. An alternative expression for $D(x)$, which is free of this restriction, can be derived from a balance of the dynamic forces due to the fluid motion at the upper surface (McKenzie *et al.* 1974; McKenzie 1977). Assuming mechanical equilibrium at the upper surface, the normal stress must vanish. For small perturbations of the upper surface from horizontal, this requires

$$-P_0 = P_1 - 2\rho\nu \frac{\partial w}{\partial z} \tag{33}$$

where P_0 is the hydrostatic pressure which would occur in the absence of motion, P_1 is the dynamic pressure due to fluid motions and w is the vertical component of velocity. Since $P_0 = \rho g d(1 - z/d)$ and $w = \partial\Psi/\partial x$, if the equilibrium surface is at $z = d + \xi$, then from (33) we have

$$\xi(x) = \frac{P_1(x, d)}{\rho g} - \frac{2\nu}{g} \left.\frac{\partial^2 \Psi}{\partial x \partial z}\right|_{z=d}. \tag{34}$$

$P_1(x, d)$ is obtained by integrating the horizontal component of the momentum equation (see McKenzie *et al.* 1974) so that (34) becomes

$$\xi(x) = \frac{\nu}{g}\int_0^x \left(\frac{\partial \omega}{\partial z}\bigg|_{z=d}\right) dx - \frac{2\nu}{g}\frac{\partial^2 \Psi}{\partial x \partial z}\bigg|_{z=d} + C \tag{35}$$

or

$$\xi(x) = \xi_1 + \xi_2 + C \tag{36}$$

where ω is vorticity, C is an arbitrary constant, ξ_1 represents the first term on the right side of (35) and ξ_2 the second. If the convection cell is overlain with water of density ρ_w then ξ is amplified by a factor of $\rho/(\rho - \rho_w)$ and the increase in water depth across the cell is therefore

$$D_2(x) = \frac{\rho}{\rho - \rho_w}[\xi(0) - \xi(x)]. \tag{37}$$

$D_2(x)$ is derived from a consideration of the dynamics of fluid flow, whereas $D_1(x)$ derives from a consideration of the resulting thermal structure. Unlike equation (32), equation (37) is exact at all x, for any Rayleigh number. It does not break down in the vicinity of the plumes and does not require any assumptions about isostasy and the corresponding depth of compensation. We can thus use $D_2(x)$ to assess the validity of the assumptions involved in deriving $D_1(x)$.

The variations of ξ and of the separate contributions to ξ (given on the right side of 36) across the upper surface of a convection cell are shown in Figs 13(a) and (b) for $R_B = 50R_c$ and $R_B = 10^4 R_c$ respectively. ξ_1 is the contribution due to non-hydrostatic pressures while ξ_2 is that due to deflection of the streamlines. At low Rayleigh numbers ξ_2 is smaller than, but comparable to, ξ_1 across most of the upper surface (Fig. 13a). However, at high Rayleigh numbers, ξ_2 is confined to the vicinity of the plumes and is essentially zero across the central portion of the cell. Consequently, at high Rayleigh numbers $\xi \approx \xi_1$, except near the plumes (Fig. 13b). In the limit $\xi = \xi_1$ we can show that within the context of boundary layer theory equation (37) reduces to a form very similar to (32).

Since ξ_2 does not vanish at $x = 0$ we can write

$$D_2(x) - \xi_{20} = \frac{-\rho\nu}{g(\rho - \rho_w)}\int_0^x \left(\frac{\partial \omega}{\partial z}\bigg|_{z=d}\right) dx \tag{38}$$

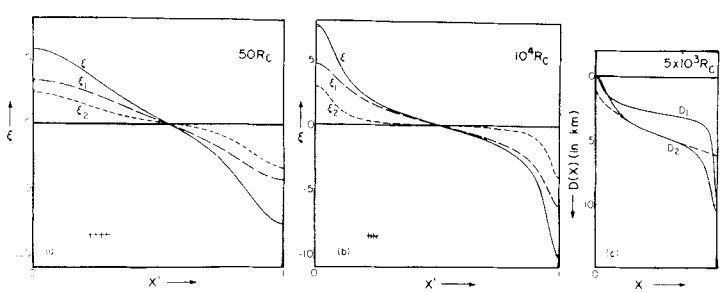

Figure 13. Topography ξ(in km) and components ξ_1 and ξ_2 (see equation 36) produced at the upper surface of convection cells when: (a) $R_B = 50R_c$ and (b) $R_B = 10^4 R_c$. (c) Comparison of bathymetric variation $D_1(x)$ predicted by (32) and $D_2(x)$ computed from (37) when $R_B = 5 \times 10^3$. The dashed line varies linearly with $x^{1/2}$. Dimensional values were obtained using values of physical parameters appropriate to whole mantle convection. For upper mantle convection the ordinate scales should be multiplied by 2.06 in (a) and (b) and by 2.25 in (c).

where ξ_{20} represents $(\rho/\rho - \rho_w)\,\xi_2(x=0)$, a constant. (This equation does not apply in the vicinity of the two plumes.)

Within the thermal boundary layer the momentum equation may be written as

$$\frac{g\alpha}{\nu}\frac{\partial T}{\partial x} = \nabla^2\omega \approx \frac{\partial^2\omega}{\partial z^2} \tag{39}$$

and hence

$$\left.\frac{\partial\omega}{\partial z}\right|_z = \frac{g\alpha}{\nu}\int_{d-z_1}^{z}\frac{\partial T}{\partial x}\,dz + \frac{1}{\rho\nu}\left.\frac{\partial P_1}{\partial x}\right|_{z=d-z_1} \tag{40}$$

where $d - z_1$ is the depth below which $\partial T/\partial x \approx 0$. Substituting (40) into (38) gives

$$\begin{aligned} D_2(x) - \xi_{20} &= \frac{\rho}{(\rho-\rho_w)}\left[-\alpha\int_0^{z_1}\left(\int_0^x\frac{\partial T}{\partial x}\,dx\right)dz^* - \frac{1}{\rho g}\int_0^x\left(\left.\frac{\partial P_1}{\partial x}\right|_{z=d-z_1}\right)dx\right] \\ &= \frac{\rho}{(\rho-\rho_w)}\left[\alpha\int_0^{z_1}[T(0,z^*) - T(x,z^*)]\,dz^* + \Delta^-\xi_1\right] \end{aligned} \tag{41}$$

where z^* is measured vertically downwards from the upper surface and $\Delta^-\xi_1 = [\xi_1(0) - \xi_1(x)]\,|_{z=d-z_1}$. A similar equation was used by Schubert *et al.* (1978), and Yuen, Tovish & Schubert (1978). Identifying ρ with ρ_m, equation (41) may be written as

$$D_2(x) = D_1(x) + D_3(x) + \xi_{20} \tag{42}$$

where $D_3(x) = [\rho/(\rho-\rho_w)]\,\Delta^-\xi_1$ represents the departure from horizontal of the level of constant vertical stress at a mean depth z_1 below the upper surface. In boundary layer theory it is assumed that ω and T are constant in the central core of the convection cell. Hence, from eqations (40)–(42) we have $D_3(x) = 0$, in which case equation (42) predicts that the variation of $D_1(x)$ equals that of $D_2(x)$ in the central region. It is therefore instructive to compare the bathymetry as computed by equations (32) and (37) for a high Rayleigh number convection model. In Fig. 13(c), $D_1(x)$ and $D_2(x)$ are plotted for a model with $R_B = 5\times10^3 R_c$. The reference $x^{1/2}$ curve fit to $D_2(x)$ illustrates an approximate $x^{1/2}$ dependence of $D_2(x)$ in the central region. Although $D_1(x)$ also varies as $x^{1/2}$ (Fig. 12b) the absolute depths are significantly different along the two curves and $D_2(x) - D_1(x)$ is not constant. The coefficients of the reference curves fit to $D_1(x)$ and $D_2(x)$ differ by a factor of about two, which implies that $D_3(x)$ is comparable to $D_1(x)$, rather than vanishingly small as required by boundary layer theory. Thus in the derivation of equation (32) the assumption of isostatic compensation below the boundary layer (i.e. $D_3(x) = 0$) introduces an error of about 100 per cent. Therefore the conclusion of the analysis in this section is similar to that reached previously for the Nusselt number: boundary layer theory predicts the correct power-law dependence of bathymetry on distance but not the absolute values.

3.6 LOCAL ENERGY BALANCE WITHIN THE VERTICAL PLUMES

In this section we briefly examine the thermal structure of a rising vertical plume. The characteristic shape of the plume, as defined by the location of the mean temperature isotherm, is shown in Fig. 14(a) for $R_B = 10^3 R_c$. The vertical arrow indicates the direction of the flow and the centre line of the plume. The tail of the arrow indicates the height at which the plume is narrowest. The horizontal component of velocity, towards the plume axis in the lower half of the cell, constrains the plume to be relatively narrow in this region. Moving upwards from the base of the arrow, the plume broadens diffusively as horizontal velocities

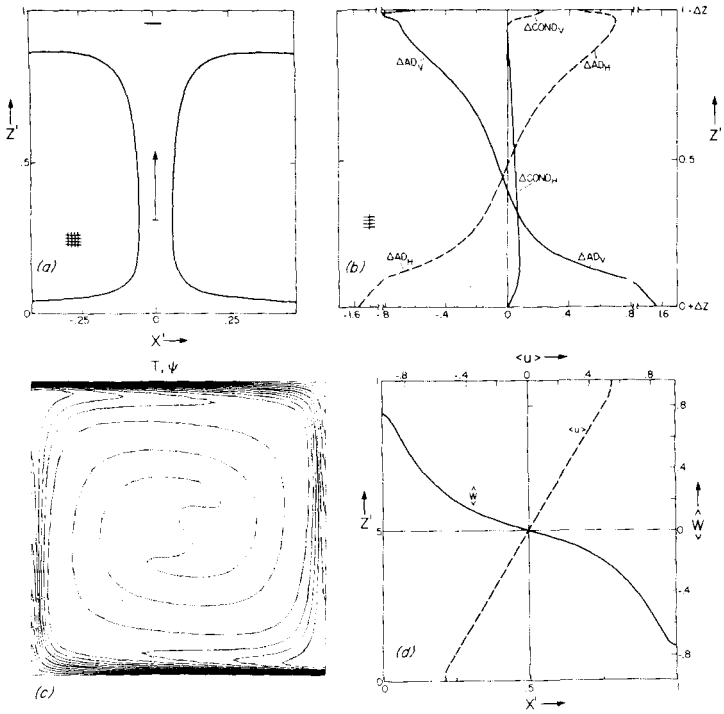

Figure 14. Characteristics of the rising plume when $R_B = 10^3 R_c$. (a) Shape of plume as defined by the isotherm ($T_d + \Delta T/2$), that is the mean temperature contour. Direction of flow is upwards. Depth of the stagnation point thermal boundary layer is indicated by the horizontal bar above the arrow on the plume axis. Steady solution obtained on a 96 × 96 finite-difference grid. (b) Contributions of the dimensionless flux components to the local energy balance plotted as a function of vertical distance along the centre-plane of the rising plume. (Δz is the vertical grid spacing. Notation as in Fig. 9.) (c) Superimposed isotherms (heavy solid curves and streamlines (light dotted curves). (d) Horizontal variation of mean dimensionless vertical velocity $\hat{W}$ (solid line) and vertical variation of mean dimensionless horizontal velocity $\langle u \rangle$ (dashed line). ($\hat{W}$ represents the vertical average of a quantity.)

initially decrease and then change sign. In the uppermost regions diverging horizontal flow sweeps the isotherms horizontally. The horizontal bar on the plume axis (above the arrow) indicates the depth of the thermal boundary layer above the diverging flow. Below the arrow in Fig. 14(a) the plume width increases with depth, in spite of larger horizontal velocities. This is a consequence of the higher central temperatures of the plume near the bottom of the cell (see Fig. 3a, for example).

An examination of the local energy balance within the plume, in the manner described in Section 3.3 for the horizontal boundary layers, has revealed that the energetic balance may be expressed as

$$\Delta AD_V + \Delta AD_H \approx 0;$$

that is, vertical advection is balanced primarily by horizontal advection (Fig. 14b). Horizontal conduction plays a very minor role in the central 15–20 per cent of the plume and is negligible elsewhere. This result invalidates the assumption, that vertical advection is balanced by horizontal conduction, which was employed in the boundary layer theory of Turcotte & Oxburgh (1967) and Oxburgh & Turcotte (1978).

The recent approach to boundary layer theory taken by Roberts (1977, 1979) and Olson & Corcos (1980) avoids this assumption. In these studies it is assumed that advection along

streamlines is balanced by diffusion across streamlines. This assumption is only rigorously true when streamlines and isotherms are parallel. Fig. 14(c) shows that this is a reasonable approximation except at the stagnation points below the sinking plume and above the rising plume. In these zones isotherms and streamlines are almost orthogonal. Since these are the regions where conduction of heat into and out of the convecting fluid is largest, the boundary layer theory prediction of the temperature profile through the upper thermal boundary layer may be unreliable at the axis of the rising plume. Errors introduced in this manner are advected downstream so that, although the *variation* of temperature throughout the boundary layer may be accurately predicted, the temperatures themselves may not be quantitatively correct. This may account for the 40 per cent discrepancy between the values of $Nu/Ra^{1/3}$ predicted by the boundary layer theory of Roberts (1979) and numerical calculations of Straus (1972) and Moore and Weiss (1973). In this regard it would be useful to compare local temperature profiles generated by boundary layer theory and direct numerical integration.

As a final point in this discussion we illustrate the effects of the torque produced by the buoyancy forces in the plumes in terms of the mean vertical and horizontal velocity profiles (Fig. 14d). Whereas the vertical gradient of horizontal velocity varies little across the depth of the cell the horizontal gradient of vertical velocity increase noticeably towards the plumes.

3.7 EFFECTS OF INTERNAL HEATING

We will now turn to investigate the effects of partial internal heating on the thermal structure of the upper boundary layer. This is of particular relevance to the geophysical problem since radiogenic elements are believed to be distributed throughout the mantle and are commonly assumed to be the agency which is most important in driving the mantle circulation. Since the actual distribution of the radioactive elements in the mantle is not known, we will consider only the simple case in which the heat sources are uniformly distributed.

The degree of internal heating in the model is determined by the parameter μ, defined in equation (14), which expresses the total rate of heat generation within the box of fluid as a fraction of the total heat flux across the upper surface of the box. Thus, when $\mu = 0$, heating is entirely from below, and when $\mu = 1$ heating is entirely from within. In order to prescribe μ we must apply a constant heat flux boundary condition at the lower surface and use the Rayleigh number R_R defined in equation (16) to characterize the model solutions.

When $\mu = 0$, for a given R_R the main features at the upper surface will be the same as for the Bénard convection models examined above but with a value of R_B determined by relation (21). When $\mu > 0$, buoyancy is generated throughout the fluid and all fluid elements attempt to circulate through the upper boundary layer in order to deliver their heat to the surface. Boundary layer theory cannot be employed to address problems concerning the properties of such a flow because heat transfer is *not* confined to boundary layers. Numerical solutions, however, can be used to determine the departure of such flows from the boundary layer behaviour of heated-from-below convection.

Upwelling of hot material from the interior of internally heated convection cells provides an additional advective component of heat transfer into the thermal boundary layer. Since vertical advection was found to play a major role in the energy balance of the boundary layers (Section 3.3) we can expect that this will produce a particularly significant effect on the thermal structure of flows in which internal heating is important.

In Fig. 15 streamlines are plotted for three different numerical models to show how the horizontal distribution of near surface vertical advection depends on both μ and R_R. At low

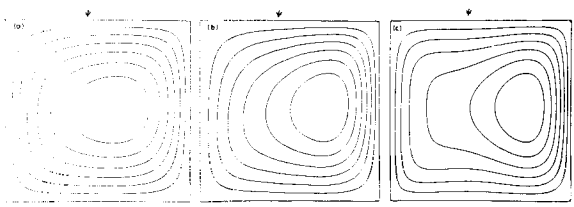

Figure 15. Streamlines (i.e. contours of constant Ψ) of steady convective circulation. (a) $R_R = 6 \times 10^5$; $\mu = 0.20$. Dimensionless contour interval $\Delta\Psi'$ is 0.0341. Solution obtained on a 24×24 grid. (b) $R_R = 6 \times 10^5$; $\mu = 0.60$; $\Delta\Psi' = 0.0267$; 24×24 grid. (c) $R_R = 1.25 \times 10^7$; $\mu = 0.20$; $\Delta\Psi' = 0.100$; 96×96 grid. Circulation is clockwise in all cases. (Dimensional values may be obtained by multiplying $\Delta\Psi'$ by $228.7\,\kappa$.)

Rayleigh numbers with $\mu = 0.20$ (Fig. 15a) there is little visible effect of internal heating on the streamlines; the flow is fairly symmetric. However, when μ is increased to 0.60 (Fig. 15b) the centre of the circulation is shifted towards the downgoing plume resulting in a broad region of relatively uniform upwards velocity. The centre of circulation can be shifted to the same degree by increasing the Rayleigh number and keeping $\mu = 0.2$ (Fig. 15c). However, unlike the solution shown in Fig. 15(b), most of the heat is transferred across the convection cell by the rising plume at the left. Vertical velocities in the interior of these cells are largest close to the descending plumes. The asymmetric flow structure which is characteristic of convection driven by internal heat sources was first observed experimentally in vertical cross sections through the circulation by de la Cruz (1970, 1973). Previously Tritton & Zarraga (1967) also noted from observed planforms that regions of descending fluid were more localized than those of ascending fluid.

3.7.1 Thermal structure of the upper boundary layer

The impact of this asymmetry on the temperature and flow structure within the thermal boundary layers is illustrated in Fig. 16. Here the vertical coordinate has been exaggerated and we have overlain isotherms and streamlines. When heating is from below ($\mu = 0$; Fig. 16a) streamlines in the central region are approximately horizontal and the spacing between isotherms increases smoothly with x (approximately as $x^{1/2}$). When $\mu = 0.6$, at a low Rayleigh number, streamlines have a vertical component (upwards) across most of the boundary layer and consequently the spacing between isotherms increases slowly (Fig. 16b). This, combined with a weak upwelling plume, produces a more uniform surface heat flow. The model with $\mu = 0.20$ and large R_R (Fig. 16c) exhibits features common to both of the previous models. At the left hot material arrives at the surface from a dominant thermal plume and then cools as it drifts to the right. Streamlines are almost horizontal and isotherm spacing increases approximately as $x^{1/2}$. To the right of centre, buoyant material arrives from the interior of the convection cell, advecting heat towards the upper surface. Streamlines bend upwards and isotherms level in this region. This initial simple cooling behaviour followed by internal heating effects is of particular geophysical interest because of the influence which it produces upon the surface topography and heat flow (Section 3.7.2).

The local energy balance one grid-plane below the upper surface is plotted in Fig. 17(a) for the model solution with $R_R = 1.25 \times 10^7$ and $\mu = 0.20$, shown previously in Figs 15(c) and 16(c). This diagram should be compared with that shown in Fig. 9(c) for a heated from below model with $R_B = 10^3 R_c$. To the right of centre, vertical advection is the major component in the local energy balance and produces a net influx of energy into each volume

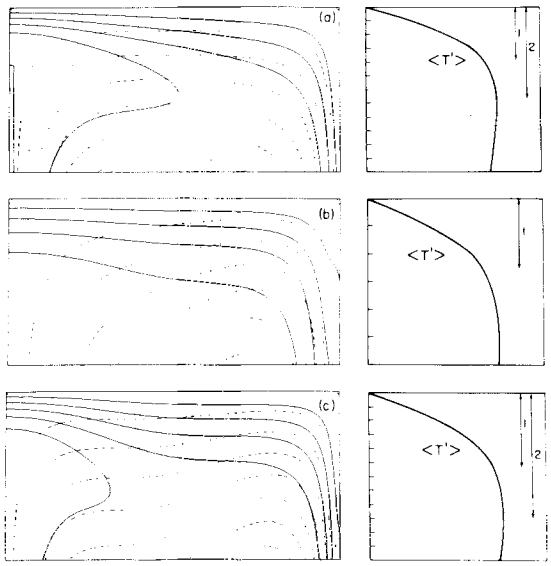

Figure 16. Superimposed isotherms (——) and streamlines (----) within the thermal boundary layer, with the corresponding variation of $\langle T' \rangle$ juxtaposed for: (a) $R_R = 1.25 \times 10^7$, $\mu = 0.0$, 96×96 grid, vertical exaggeration of 4; (b) $R_R = 6 \times 10^5$, $\mu = 0.6$, 24×24 grid, vertical exaggeration of 2; (c) $R_R = 1.25 \times 10^7$, $\mu = 0.20$, 96×96 grid, vertical exaggeration of 4. Grid intervals are indicated at the left margin of the $\langle T' \rangle$ graphs. The depths indicated by the labels 1 and 2 correspond to the boundary layer thicknesses δ_1 and δ_2 respectively as defined in Fig. 5. (Contour intervals are equal for parts a and c.)

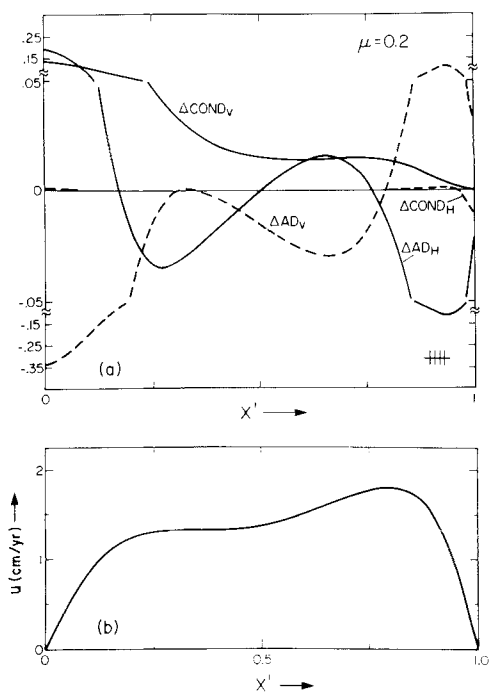

Figure 17. (a) Contributions of the dimensionless flux components to the local energy balance plotted as a function of horizontal distance x' one grid-plane below the upper surface. $R_R = 1.25 \times 10^7$; $\mu = 0.20$; 96×96 grid. Notation as in Fig. 9(c). (b) Variation of horizontal velocity across the upper surface of the same convection cell as in (a) dimensionalized using values in Table 1.

element. (In contrast, when heating is entirely from below, horizontal advection is the major component and vertical advection produces a net outflow of energy from each volume element.) In Fig. 17(a) we see that the large influx of energy due to vertical advection (to the right of centre) is partially offset by a change in sign of the contribution due to horizontal advection. The sign change in ΔAD_H is due to the increase in horizontal velocity in this region (Fig. 17b) which is required in order to conserve mass.

3.7.2 Heat flow and topography

The change in thermal structure of the boundary layers due to the asymmetric flow, which occurs when heating is partially from within, is sufficient to produce major departures from the power law variations of F_u, the surface heat flow, and of $D(x)$, the bathymetry, discussed above. In Fig. 18 $D(x)$ and $F_u(x)$ are plotted for various values of μ with R_R held constant at a relatively low value. Both expressions for bathymetry $D_1(x)$ and $D_2(x)$ are shown for comparison. At $\mu = 0$, F_u varies approximately as $x^{-1/2}$; as μ increases from 0.0 to 1.0, F_u becomes more uniform and loses its $x^{-1/2}$ dependence. Since $D(x)$ is an integrated effect it is less sensitive to μ at this value of R_R and departures from an $x^{1/2}$ dependence are not extreme. (This is partially due to the extra degree of freedom in fitting the reference curves to bathymetry.) However, to the right of centre, as μ increases, the bathymetry increases more slowly than the power-law reference curves. This is a direct consequence of the additional heat advected into the base of the boundary layer for $\mu > 0$. We define P, the percentage 'flattening' of the bathymetry profiles, as the maximum difference between the model bathymetry curve and the reference curve, expressed as a percentage of the value on the reference curve. For a fixed R_R, P is an increasing function of μ. (At larger Rayleigh numbers the dependence of P on μ is more pronounced, but steady solutions cannot be obtained for all values of μ.) At such low Rayleigh numbers $D_1(x)$ (Fig. 18c) exaggerates the amount of flattening in the actual bathymetry, $D_2(x)$ (Fig. 18a).

In Fig. 19 a sequence of bathymetry and surface heat flow profiles are shown for three values of R_R with $\mu = 0.20$ in each case. Fig. 19(a) shows that P increases with R_R while Fig. 19(b) indicates that the heat flow variation is not very sensitive to changes in R_R. Thus, at $R_R = 1.25 \times 10^7$ and $\mu = 0.20$, the bathymetry varies as $x^{1/2}$ to the left of centre and flattens by an amount $P \approx 19$ per cent to the right of centre, while the heat flow departs little from an $x^{-1/2}$ behaviour. At lower values of R_R and higher μ the same value of P can be

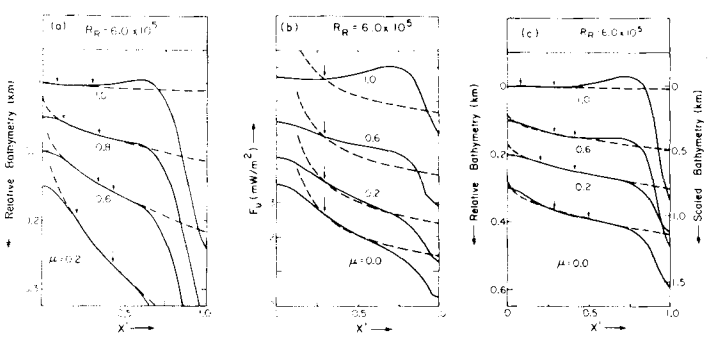

Figure 18. Horizontal variations of (a) bathymetry $D_2(x)$, (b) surface heat flux F_u and (c) bathymetry $D_1(x)$, across model convection cells at $R_R = 6.0 \times 10^5$ and a range of values of μ as indicated on the graphs. Curves are offset at the origin for clarity. Solid curves are the model predictions and dashed curves are the appropriate reference curves fit to the model curves at the points indicated by the arrows. Variables have been dimensionalized using parameter values from Table 1.

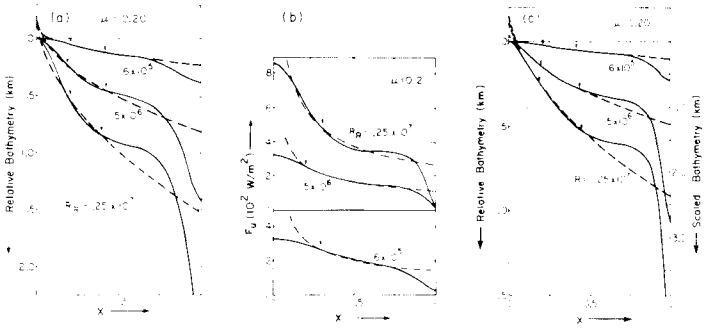

Figure 19. Horizontal variations of (a) bathymetry $D_2(x)$, (b) surface heat flux F_u and (c) bathymetry $D_1(x)$, across model convection cells with $\mu = 0.20$ and a range of R_R as indicated next to the individual curves. Profiles are not offset here. Solid curves are the model predictions and dashed curves are the appropriate reference curves fit to the model curves at the points indicated by the arrows. Variables dimensionalized using parameter values from Table 1.

obtained but F_u departs considerably from an $x^{-1/2}$ power law curve. This is due to the different streamline pattern for the two cases as discussed above with reference to Figs 15 and 16. Profiles of $D_1(x)$ shown in Fig. 19(c) can be compared with those of $D_2(x)$. Although the absolute values of bathymetry differ considerably the values of percentage flattening obtained from profiles of either $D_1(x)$ or $D_2(x)$ differ little from one another at this relatively high Rayleigh number.

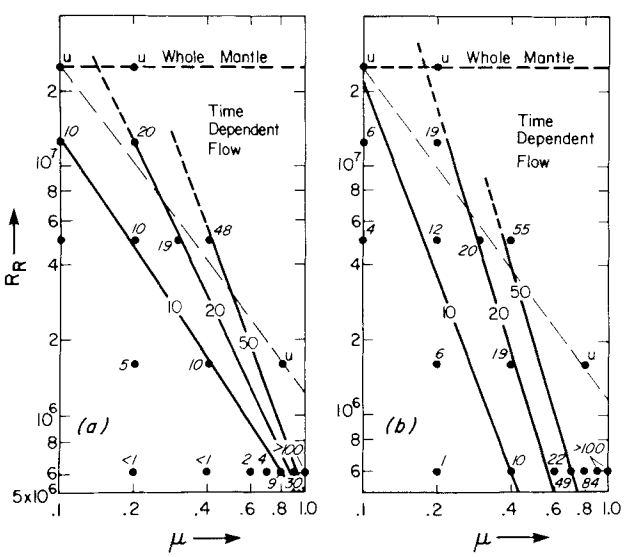

Figure 20. Domain diagrams on which percentage flattening P is plotted as a function of R_R and μ. Solid circles indicate the (R_R, μ) coordinates for which values of P were obtained and the adjacent numbers give the values of P (in per cent). Approximate contours of constant P are shown for $P = 10$, 20, and 50 per cent. The broken diagonal *roughly* divides domains of steady and non-steady single cell flows: Steady single-cell solutions can be obtained at points below the line, time-dependent (or multi-cell) solutions above. Points for which solutions were too unsteady to compute meaningful values for P are indicated by *Us*. The horizontal broken line at $R_R = 2.5 \times 10^7$ indicates our estimate of R_R for whole mantle convection. The model solutions were obtained on finite-difference grids of 24×24 intervals for $R_R \leqslant 6 \times 10^5$, 48×48 for $R_R = 1.6 \times 10^6$, 64×64 for $R_R = 5 \times 10^6$ and 96×96 for $R_R \geqslant 1.25 \times 10^7$. (a) Values of P determined from profiles of $D_2(x)$. (b) Values of P determined from profiles of $D_1(x)$.

The joint dependence of P on both μ and R_R is summarized in the domain diagrams shown in Fig. 20. Here P is plotted as a function of μ and R_R. Values of P are indicated for the states examined and manually drawn contours of P indicate the trends. For a given amount of flattening, the value of μ required is a decreasing function of R_R. Fig. 20(a) results from determining P from profiles of $D_2(x)$ while Fig. 20(b) results from estimating P from profiles of $D_1(x)$. Comparing the two indicates that although Fig. 20(b) overestimates P at low Rayleigh numbers, it gives similar results to Fig. 20(a) at high Rayleigh numbers. This point has been alluded to previously by Jarvis & Peltier (1980).

4 Summary of numerical results and discussion of their geophysical implications

Our numerical simulations of two-dimensional convection in constant viscosity fluids show that the power-law dependence of such quantities as the Nusselt number and the thermal boundary layer thickness on the (appropriately defined) Rayleigh number agrees reasonably well with the predictions of boundary layer theory. The coefficients of proportionality which determine the absolute values of these quantities appear, however, to be correct only to within a factor of approximately two. The variations of heat flow and topography across the upper surface of heated from below convection cells also approximate the power law dependence upon x predicted by boundary layer theory. In the case of the surface heat flux, this agreement is due primarily to the fact that three large but competing effects which are often ignored in boundary layer theories tend to cancel one another. The most important of these effects is the vertical advection of heat into and out of the upper thermal boundary layer. This influence is partially compensated by the related effect of non-zero $\partial u/\partial x$ in the boundary layer. The third effect is that due to the lack of singularity in the heat flow above the rising plume, which prevents the computed heat flow from exceeding that predicted by blt in spite of the predominance of vertical advection in the local energy balance. As there is no similar mitigating influence above the cold descending plume, vertical advection results in an increasing departure from the boundary layer prediction in this region (see, e.g. Fig. 12). Reference curves which depend linearly upon $x^{1/2}$ fit the model predictions of topography very well, although the absolute heights disagree with blt predictions by a factor of two or more. This discrepancy may be attributed to an x dependence of the depth of compensation in a convective circulation. In a static system (isostatic) compensation is effected at a constant depth whereas, in a dynamic system (isobaric) compensation occurs along a surface of constant normal stress. The 'relief' of this isobaric surface in a convection cell with an aspect ratio of one is comparable to that due to thermal contraction of the overlying thermal boundary layer.

Since boundary layer theory is applicable only in the limit of very high Rayleigh numbers, our comparisons between the numerical model and the predictions of blt for surface heat flow and topography (Sections 3.4 and 3.5) were made for the highest Rayleigh number for which adequate numerical resolution could be achieved ($R_B \approx 5 \times 10^3 R_c$), which is most appropriate to the whole mantle convection model. For lower Rayleigh numbers, such as those appropriate to upper mantle convection models, the discrepancies noted above between the numerical results and blt are *more* pronounced. These discrepancies are primarily due to the important effects of the vertical advection of heat on the boundary layer energy budget.

Rayleigh numbers appropriate to upper mantle and whole mantle convection both lie well within the boundary layer regime of the numerical calculations. Consequently, if heating were entirely from below ($\mu = 0$) we would expect small departures from boundary layer behaviour. It is generally assumed, however, that μ must be greater than zero due to the presence of heat producing radioactive elements within the convecting region. Our model

results show that significant departures from the predictions of heated from below boundary layer theory do occur for convection cells which are partially heated from within. We will proceed, therefore, to consider the geophysical implications of $\mu > 0$ both in the context of upper mantle convection and in the context of whole mantle convection.

4.1 UPPER MANTLE CONVECTION

Models of convection in the upper mantle may be divided for our purposes into two basic categories, which we shall refer to as 'large scale' and 'small scale' and which are illustrated in Figs 21(a) and (b) respectively. In the large-scale model it is assumed that the convective circulation takes the form of large aspect ratio Bénard-like convection cells with a hot rising plume beneath oceanic ridges and a corresponding cold descending plume associated with the deep oceanic trenches (e.g. Turcotte & Oxburgh 1967, 1972). In this model it is assumed that the circulation is restricted to the region above the seismic discontinuity at 670 km depth and that the oceanic lithosphere is to be associated with the thermal boundary layer itself. Below the lithosphere is an extremely elongate isothermal core. In order to achieve the large aspect ratios required to account for surface plate dimensions, it is assumed that the rigidity of the lithosphere (due to the temperature-dependence of viscosity) stabilizes the cells with respect to aspect ratio one disturbances. It is also conceivable, in this picture, that the scale of the upper mantle flow associated with plate creation and destruction might be governed by that of a distinct circulation in the underlying lower mantle (Busse 1981).

In the small-scale upper mantle model illustrated in Fig. 21(b), it is assumed that convection is occurring beneath a rigid lithosphere and that this circulation has a horizontal scale comparable to the depth of the upper mantle (Richter 1973b; McKenzie *et al.* 1974; Richter & Parsons 1975). The many small cells maintain an almost isothermal region below the lithosphere except for the hot and cold plumes associated with the small-scale circulation. In this model, oceanic ridges are zones of plate divergence and are not in general associated with

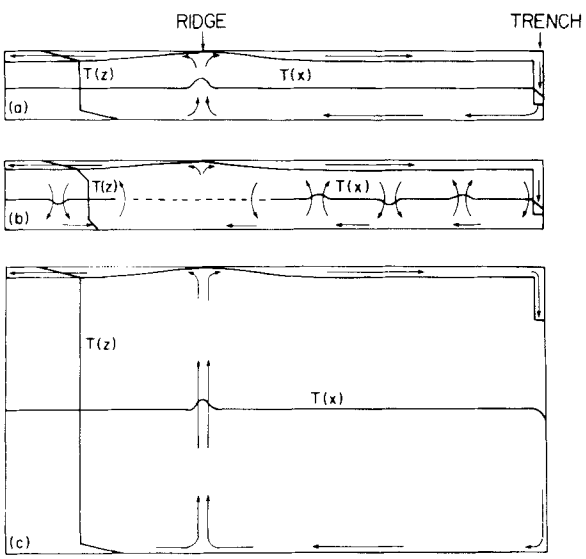

Figure 21. A comparison of three models of mantle convective circulation involving the lithospheric plates. (a) The lithosphere forms the thermal boundary layer of an upper mantle convective circulation. (b) The lithosphere moves above a smaller-scale convective circulation. (c) The lithosphere forms the thermal boundary layer of a mantle-wide convective circulation.

rising plumes of the small-scale circulation. As the plates move apart magma is tapped from the underlying convecting zone. A return flow from trench to ridge is superimposed on the small-scale flow as required by mass conservation and this might be weak if the lithosphere were mechanically decoupled from the mantle below by a thin low viscosity channel (Richter & McKenzie 1978). In this model, the driving mechanism for the observed plate motions is not associated with the small-scale convection. Rather, it is assumed (and some justification for this assumption is provided by Richter & McKenzie 1978) that buoyancy forces localized at ridge crests and ocean trenches maintain the plate motions.

The two versions of upper mantle convection may be compared from the point of view of their predictions regarding surface heat flow and ocean floor bathymetry. In the large-scale upper mantle model, when $\mu = 0$ surface heat flux is entirely due to the cooling of the initially hot plume material as it drifts horizontally away from the ridge. There is virtually no heat delivered to the base of the thermal boundary layer and thus cooling continues across the length of the plate with heat flow decreasing as $x^{-1/2}$ and bathymetry increasing as $x^{1/2}$. In this model the rheological lithosphere and the thermal boundary layer of the convective circulation are coincident, the high effective viscosity of the lithosphere arising as a consequence of the strong temperature dependence of viscosity. Qualitatively, our previously discussed numerical results suggest that with $\mu > 0$ additional heat will be advected to the base of the lithosphere and thus reduce the rate of thermal contraction. Our analyses, however, cannot be employed to make any quantitative assessment of the magnitude and distribution of this effect because of the wide disparity between the high aspect ratios required in this model of upper mantle convection and the aspect ratio one cells to which all our numerical results pertain.

In the small-scale upper mantle model, when $\mu = 0$ the surface heat flux is due to cooling of the intruding magma as it moves away from the ridge crest plus the background heat flux due to the small-scale convection in the upper mantle beneath the lithosphere. Although the upper thermal boundary layer of each small cell cools approximately as predicted by boundary layer theory, the large number of cells and the relatively small variation of heat flux across each produces an approximately uniform heat flux into the base of the lithosphere. Cooling of the lithosphere (and the consequent thermal contraction) continues until the surface heat flux due to cooling of the horizontally moving lithosphere equals that delivered to the base of the lithosphere due to the small-scale convection below. Even with $\mu = 0$, this model therefore predicts that surface topography will flatten away from an initial $x^{1/2}$ variation (Parsons & McKenzie 1978). With $\mu > 0$ there would be asymmetries induced in the small-scale convection cells but this would produce only relatively short wavelength effects. In this model surface heat flow and topography are therefore relatively insensitive to the degree of internal heating.

In both large- and small-scale upper mantle models, the implied ocean floor bathymetry initially varies as $x^{1/2}$. With an appropriate choice of physical parameters, this topographical variation can be accounted for by thermal contraction if one assumes isostatic compensation at the base of the lithosphere (Parsons & Sclater 1977; Oxburgh & Turcotte 1978). However, the numerical models demonstrate that compensation does not occur at a constant depth in a dynamic flow. For the large-scale upper mantle model this may produce a significant contribution to the surface topography. Attempts to fit the observed topography with the thermal contraction model could therefore lead to erroneous estimates of the relevant physical parameters of the lithosphere. Although our numerical solutions show that this error could be as large as 100 per cent for aspect ratio one cells, we cannot extrapolate this result to the large-scale upper mantle model which requires much larger aspect ratios than this. We simply point out that this effect may be another source of error and should therefore be considered when the large-scale model of upper mantle convection is employed. For

the small-scale upper mantle model, variations in the depth of compensation occur with a much shorter wavelength than that corresponding to the overall variation of topography. No systematic variation occurs over the length of the plate and hence the assumption of a constant depth of compensation is more appropriate.

4.2 WHOLE MANTLE CONVECTION

A whole mantle alternative to the upper mantle convection models discussed above is illustrated schematically in Fig. 21(c). In this model the lithosphere is identified with the thermal boundary layer of a large-scale convective circulation which itself extends to the core–mantle boundary. Hot plumes rise beneath ocean ridges and cold plumes sink beneath ocean trenches (in the manner envisioned originally by Hess 1962, and recently advocated on the basis of quantitative considerations by Sharpe & Peltier 1978, and Peltier 1980). As in the large-scale upper mantle model, the rigidity of the lithosphere is assumed to provide stability with respect to smaller scale circulation, although in the whole mantle model the largest aspect ratio required to account for surface motions is only about three. One difficulty in applying the numerical results to the whole mantle model concerns the neglect of geometric curvature in the numerical calculations. Fig. 22 illustrates the degree of misfit of the computational domain with aspect ratio one and a slice of the Earth's mantle of width 2900 km at mid-depth. In applying numerical results to this model it is implicitly assumed that convection in the square domain approximates that in the curved mantle wedge. For an aspect ratio of one this assumption does not seem unreasonable, particularly in view of the fact that the direction of gravity remains normal to the bounding surfaces. For aspect ratios as large as three this assumption becomes suspect, although numerical solutions obtained in spherical coordinates (Hsui, Turcotte & Torrance 1972; Young 1974; Zebib, Schubert & Strauss 1980) show few qualitative differences from those in Cartesian coordinates. The main effect is an increasing heat flux with depth, to account for the decreasing surface area

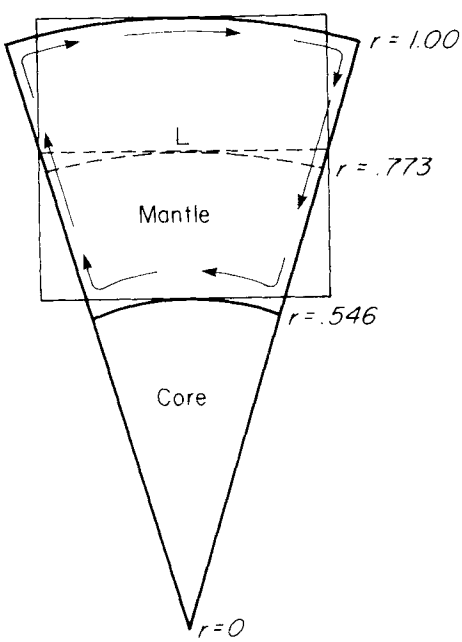

Figure 22. Misfit of square computational domain and wedge of whole mantle with horizontal dimension at mid-depth equal to 2900 km (the depth to the core–mantle boundary).

of concentric spherical shells, which results in a larger temperature difference across the lower thermal boundary layer than that across the upper since the boundary layer thicknesses are found to remain approximately equal.

In the whole mantle model an adiabatic core rotates passively. When $\mu = 0$ heat flows across the mantle primarily through the vertical plumes at the edges of the convection cell. There is no (superadiabatic) background heat flux from the mantle away from the plumes and consequently surface heat flux and topography vary as $x^{-1/2}$ and $x^{1/2}$ respectively. When $\mu > 0$ the numerical results discussed above suggest that, at low values of μ, the departure of the surface heat flow variation from that when $\mu = 0$ is relatively small. In contrast, even small amounts of internal heating produce a sufficient change in the thermal boundary layer structure to cause significant 'flattening' of the topographic variation compared to the $x^{1/2}$ variation found when $\mu = 0$. The initial $x^{1/2}$ variation of the cooling lithosphere can only be partially accounted for by thermal contraction; there is also a contribution from hydrodynamic pressures beneath the lithosphere. Thus, if the whole mantle convection model were correct, fitting an isostatically compensated thermal contraction model to the ocean bathymetry would lead to erroneous estimates of the physical parameters of the lithosphere.

The geophysical data most relevant to the above discussion are those for the variation of ocean floor bathymetry (e.g. Parsons & Sclater 1977). The bathymetry of both the North Pacific and North Atlantic varies initially as $t^{1/2}$, or as $x^{1/2}$ on each (constant velocity) plate. For ocean floor older than about 80–90 Ma (the approximate mid-point of both ocean basins) the bathymetry systematically flattens with respect to an $x^{1/2}$ behaviour. The percentage flattening in both cases is about 18 per cent. The small-scale upper mantle model appears to be able to account qualitatively for this behaviour regardless of the value of μ. In the context of the large-scale upper mantle and whole mantle models, the asymmetric flow structure developed when $\mu > 0$ may also account for (or at least contribute to) this behaviour. In particular we have found that, at Rayleigh numbers appropriate to the whole mantle model, a percentage flattening of $P \approx 18$ per cent is obtained in constant viscosity fluids for $\mu \approx 0.2$ (Fig. 20). The main difficulty with this interpretation is that it does not account for the similarity of the depth–age curves for the Atlantic and Pacific oceans which obtains in spite of a presumably different large-scale flow structure beneath the two. The amount of flattening achieved with relatively low values of μ and the qualitative similarity of the model and ocean floor bathymetry nevertheless suggest that internal heating may play the crucial role.

4.3 INFLUENCE OF THE LITHOSPHERIC PLATES

An important physical effect not contained in our numerical calculations, which could alter the value of μ inferred from the bathymetry in the context of the whole mantle model, is the strong temperature-dependence of viscosity. The high viscosity lithosphere behaves in a plate-like fashion such that the horizontal velocity is not a strong function of age. In Section 3.3 we have shown that convection at infinite Prandtl number in a fluid with *constant* viscosity was characterized by pronounced variation, even at very high Rayleigh numbers, of the horizontal velocity across the top of the cell (Fig. 8a). This variation results in vertical advection of heat within the thermal boundary layer. The temperature dependence of viscosity acts to suppress such variation and hence to reduce the influence of vertical advection upon the boundary layer temperature field. Since flattening due to internal heating in the convective circulation is controlled by horizontal variations of temperature within the boundary layer it would appear that, for a given proportion of internal heating, inclusion of the plate-like behaviour of the lithosphere could affect the predicted degree of flattening.

Perhaps the simplest approach to investigate the effects of suppressing $\partial u/\partial x$ in the horizontal boundary layer is to impose a constant horizontal velocity on the upper surface as a boundary condition. Viscous coupling to the underlying fluid will then suppress $\partial u/\partial x$ close to the surface. Imposing a constant surface velocity produces a shear stress on the upper boundary; hence vorticity along the upper surface, which is proportional to shear stress, no longer vanishes. Rather it must be obtained iteratively from the Ψ field (Richter 1973a; Lux, Davies & Thomas 1979).

For illustrative purposes we consider a model with $R_R = 5 \times 10^6$, $\mu = 0.20$ and a constant surface velocity, u_0, equal to the mean surface velocity which occurs for a model with the same values of R_R and μ but with free-slip boundaries. The predicted temperature, vorticity and stream function fields are compared with those of the corresponding free-slip case in Figs 23(a) and (b). The most diagnostic field is that of the vorticity, ω. The constant surface velocity u_0 is greater than that occurring near the plume in the stress free case (Fig. 23a) and less than that in the central regions. Thus, the new mechanical boundary condition produces an increase in vorticity near the vertical boundaries of the cell (drawing the contours of ω towards the corners) and a reversal of vorticity, or drag, in the central regions (close to the surface). The net effect on the streamlines is to square off the flow in the upper regions. A significant point to note from Fig. 23(b) is that the basic asymmetry of the flow persists in spite of the constant velocity of the upper boundary.

Away from the vertical boundaries the thermal field is not very sensitive to the boundary condition on the velocity field (Fig. 23). When a constant velocity is imposed at the surface, vertical advection is enhanced above the plumes (due to the increased horizontal velocities in the near vicinity) and suppressed throughout the central region. The net effect on the variation of surface heat flow, shown in Fig. 24(b), is that it now more closely approximates the $x^{-1/2}$ variation predicted by boundary layer theory and observed on the seafloor.

At large Rayleigh numbers the surface topographic variation is determined primarily by the horizontal integral of $\partial\omega/\partial z$ at the upper surface (see Section 3.3). $\partial\omega/\partial z$ is in turn the vertical integral of $\partial^2\omega/\partial z^2$ which, away from the vertical boundaries, equals $\partial T/\partial x$. Thus, the qualitative similarity of the temperature field shown in Figs 23(a) and (b) results in similar topographic variations for the two cases (Fig. 24a). In the central region the topographic profile is not significantly altered by the constant velocity boundary condition.

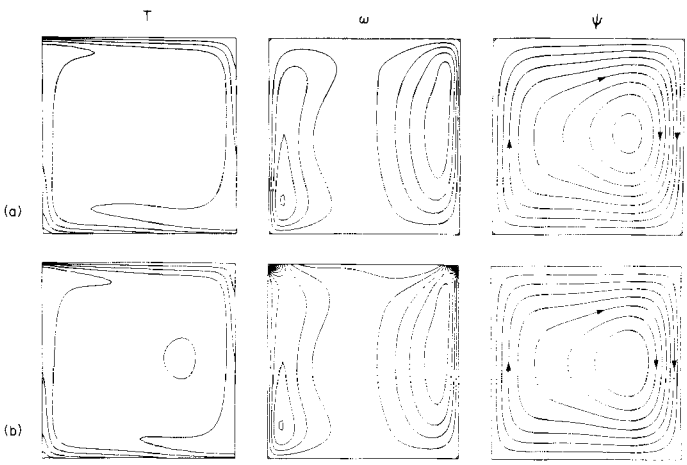

Figure 23. Contours of T (temperature), ω (vorticity) and Ψ (stream function) for $R_R = 5.0 \times 10^6$, $\mu = 0.20$. (a) Solution with free-slip boundary condition at the upper surface. (b) Solution with constant velocity boundary condition at the upper surface. Contour levels of each field are the same in (a) and (b).

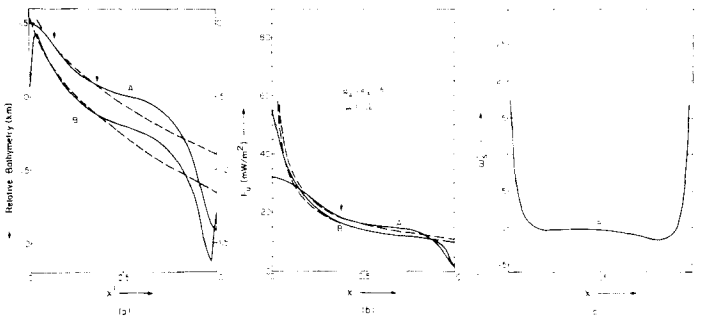

Figure 24. Comparison of (a) relative bathymetry, $D_2(x)$, and (b) surface heat flux, F_u, as computed from the model solutions with free-slip upper boundary conditions (curves labelled A) and constant velocity upper boundary condition (curves labelled B). D_2 and F_u have been dimensionalized using the parameter values listed in Table 1. In (a) the left ordinate scale refers to curve B while the right scale refers to curve A. (c) Variation of dimensionless vorticity at the upper surface, ω_s', in the case of the constant velocity upper surface.

One distinction between the two cases is the reversed topographical gradient close to the vertical boundaries when a constant surface velocity is imposed, which does not occur with the no-shear boundary condition. These reversals imply a change in sign of $\partial^2\omega/\partial z^2$. This is not possible away from the vertical boundaries where $\partial^2\omega/\partial z^2 \approx \partial T/\partial x$ and is always negative. However, near the vertical boundaries

$$\frac{\partial^2\omega}{\partial z^2} = \frac{\partial T}{\partial x} - \frac{\partial^2\omega}{\partial x^2}$$

where $\partial^2\omega/\partial x^2$ is negative, so that $\partial^2\omega/\partial z^2$ may be positive. In the vicinity of the vertical boundaries the constant surface velocity produces a large shear and hence vorticity at the upper surface (Fig. 24c). Immediately below the surface horizontal diffusion of vorticity ($\partial^2\omega/\partial x^2$) reduces the value of vorticity in spite of the vorticity source term ($\partial T/\partial x$). Consequently, surface values of $\partial\omega/\partial z$ are negative close to the vertical boundaries but positive elsewhere. This local effect is a manifestation of the unrealistically large shear stresses resulting from the imposed constant surface velocity boundary condition and cannot be expected to occur on the ocean floor. (The same topographic feature was noted by Parmentier & Turcotte 1978 near the spreading axis of their upper mantle convection model when they applied similar boundary conditions.)

A second effect excluded from the present calculations is the influence of the temperature-dependence of viscosity on the overall circulation. McKenzie & Richter (1976) have shown that in one parameter range the circulation of internally heated fluids is qualitatively the same in both constant viscosity and temperature-dependent viscosity fluids. In a different parameter range Daly (1978) finds that internally heated fluids with temperature dependent viscosity exhibit narrow upwelling and broad downwelling regions (i.e. opposite to the constant viscosity case). No variable viscosity calculations have yet been performed at the high Rayleigh numbers appropriate to the whole mantle. However, in this parameter range we find that the asymmetry characteristic of internally heated constant viscosity fluids is highly accentuated (Fig. 15), and it therefore seems possible that a narrow downwelling and broad upwelling pattern will also exist in variable viscosity flows at these high Rayleigh numbers. However, regardless of the magnitude, or sense, of asymmetry of the flow, once variable viscosity is introduced the topography is no longer simply related to the position of the centre of circulation. Thus, McKenzie (1977), for example, provides examples of heated

from below circulations in variable viscosity fluids, with narrow upwelling and broad downwelling regions, above which the topography increases away from the upwelling axis.

None of the currently available variable viscosity solutions incorporate, at Rayleigh numbers appropriate to the whole mantle, either a dependence of viscosity on homologous temperature T_m/T (where T_m is the melting temperature) (Weertman 1970), or a constant surface velocity boundary condition. It is therefore difficult to assess the role of variable viscosity within the mantle. Peltier (1980) has suggested that near surface melting could play a crucial role in regulating the system such that the high viscosity of the lithosphere itself exerts no active influence on the flow. If this were the case then the approximate incorporation of the effect of variable viscosity which we have effected here, by forcing the circulation to satisfy the constant surface velocity boundary condition, may produce a circulation not unlike that in the mantle. Our model is now similar to the two-layer model of the mantle proposed by Elsasser (1971) and employed recently by Richter & McKenzie (1978) in which a rigid lithosphere overlies a uniform viscous fluid. If this is a reasonable approximation to mantle rheology then the above results may not be sensitive to the precise functional dependence of viscosity on temperature. In this regard, the lack of geophysical evidence to indicate a broad zone of high viscosity adjacent to descending plates at subduction zones suggests that the two-layer model may in fact be the appropriate model.

4.4 PARAMETERIZED CONVECTION

The plausibility of a low value of μ in a mantle-wide convection model has important implications for planetary thermal history calculations. Sharpe & Peltier (1978, 1979), for example, assumed $\mu = 0$ as a first approximation and made use of boundary layer scaling relationships appropriate for Bénard convection in the form

$$\delta = \beta_1(a)d(R_B/R_c)^{S_1} \tag{44a}$$

$$\bar{u} = \beta_2(a)\,(\kappa/d)\,(R_B/R_c)^{S_2} \tag{44b}$$

$$\bar{w} = \beta_3(a)\,(\kappa/d)\,(R_B/R_c)^{S_3} \tag{44c}$$

$$\bar{q} = \beta_4(a)\,(K\Delta T/d)\,(R_B/R_c)^{S_4} \tag{44d}$$

$$Nu = \beta_4(a)\,(R_B/R_c)^{S_4} \tag{44e}$$

where approximate values of $\boldsymbol{\beta}$ and $\mathbf{S}$ were deduced from boundary layer theory. Exact values of $\boldsymbol{\beta}$ and $\mathbf{S}$ for an aspect ratio $a = 1$ can be computed from the curves plotted on Fig. 5 as

$$\boldsymbol{\beta} = (0.300, 8.468, 8.671, 2.30) \tag{45a}$$

and

$$\mathbf{S} = (-0.278, 0.645, 0.684, 0.313). \tag{45b}$$

A comparison of the scaling relations derived from our numerical models and boundary layer theory is shown in Table 2. Scaling relationships similar to (44) can also be written for non-zero values of μ, the coefficients and power laws again being deduced from numerical calculations (e.g. McKenzie *et al.* 1974).

In order to apply these scaling relations to the Earth's mantle, some *a priori* assumptions must be made. This is because the computed power law indices and coefficients apply strictly to two-dimensional, steady-state flows in constant viscosity fluids. Their use, therefore, involves the implicit assumption that departures from these conditions will not affect the end result. As yet these assumptions have not been justified.

Table 2. A comparison of numerical and theoretical power-law relations.

Relation	Coefficient (β_i)		Exponent (S_i)	
	Numerical	Theoretical*	Numerical	Theoretical
$\delta = \beta_1 d\,(R_B/R_c)^{S_1}$	0.300†	0.465	−0.278†	−0.333
$u = \beta_2 (\kappa/d)\,(R_B/R_c)^{S_2}$	8.468	10.813	0.645	0.666
$w = \beta_3 (\kappa/d)\,(R_B/R_c)^{S_3}$	8.671	18.98	0.684	0.666
$Nu = \beta_4 (R_B/R_c)^{S_4}$	2.30	0.93	0.313	0.333

*Coefficients in this column are from Oxburgh & Turcotte (1978) and apply strictly for an aspect ratio of 1.4 rather than 1.0.

†These values correspond to δ_1 as defined in Fig. 5. For δ_2, $\beta_1 = 0.518$ and $S_1 = -0.285$.

5 Conclusions

The foregoing discussion has been concerned with the description of numerical simulations of thermal convection through the range of Rayleigh numbers which is appropriate to the Earth's mantle. With respect to convective flows forced by heating from below, the analysis focused upon a detailed comparison of the numerical results with the predictions of boundary theory. Although boundary layer theory correctly predicts the power-law dependence of the heat transport, boundary layer thickness and typical velocities, it fails at the 100 per cent level to determine their absolute values correctly. For the purpose of thermal history modelling the exact power-law relations determined either numerically or empirically should therefore be employed rather than those obtained from boundary layer theory. Fortunately from the point of view of the prospects of such modelling, the detailed mean temperature profile exhibits a strong similarity as a function of Rayleigh number, a feature which may be employed to generate mean temperature profiles for the thermal history models.

The major new physical result, presented in Section 3.3, is the important role played by the vertical advection of heat in the local energy balance within the horizontal thermal boundary layers, of constant viscosity fluids, at all Rayleigh numbers. For steady convection cells which are heated entirely from below, a balance is maintained locally (within the horizontal boundary layers) by the horizontal *and* vertical advection and vertical diffusion of heat. Thus, when computing the local surface heat flux across the upper surface of a constant viscosity convection cell, in terms of the temperature and flow fields immediately below the surface, neither horizontal nor vertical advection should be neglected. (However, when averaging horizontally across the cell horizontal advection may be ignored since the integrated local contributions must vanish.) Contrary to this result, boundary layer theories generally assume that vertical advection is negligible in the horizontal boundary layers. Somewhat ironically this assumption appears to be more appropriate to those mantle convection models in which the rigid lithosphere forms the upper thermal boundary layer of the convective circulation than it is to the simpler case of a constant viscosity fluid.

An interesting geophysical result obtained from this work has concerned the impact of internal heating upon the boundary layer structure such as to cause increasingly marked departures from heated below flows as the Rayleigh number R_R increases, with μ fixed. These departures are most clearly seen in the topographic variation associated with boundary layer cooling. Internal heating causes the implied topography to 'flatten' away from the $x^{1/2}$ variation expected when heating is entirely from below. The geophysical implications of this result are most important if the oceanic lithosphere forms the thermal boundary layer of a mantle-wide convective circulation. If this is the case, the observed flattening of the

oceanic bathymetry profiles might be attributed to radioactive heating in the mantle. With $\mu = 0.2$ the constant viscosity model then predicts the observed amount of flattening and the approximate magnitude of topographic relief on the ocean floor.

The small-scale model of upper mantle convection also appears capable of explaining the observed bathymetry, independent of the value of μ. It is therefore only in the context of the whole mantle model that topography constrains the value of μ to be small. Although this constraint depends upon the validity of the whole mantle model it is nevertheless interesting to compare the value of $\mu = 0.2$ to independent estimates.

According to some authors (e.g. Oxburgh & Turcotte 1978; Turcotte *et al.* 1979) who believe that the convective circulation is most probably driven entirely by internal heating, $\mu = 0.2$ is an extremely low estimate. With μ as low as 0.2 the circulation is, in contrast, driven primarily by heating from below. In the context of the whole mantle model this would imply that there is a substantial heat flow across the core–mantle boundary. This implication is consistent with the thermal history calculations of Sharpe & Peltier (1978, 1979) which suggest that the heat capacity of the core is sufficiently high that the large heat transports associated with high Rayleigh number convection can be tolerated for times on the order of the age of the Earth without leading to freezing of the Earth's core. In these models the assumed mantle-wide convective circulation is driven entirely by the cooling of Earth in bulk. Although this cannot be literally true their calculations established that this energy source for the circulation could well be of predominant importance. Independent geochemical evidence has recently been forthcoming which suggests that an appropriate value of μ for the whole mantle is as low as 0.3 (O'Nions *et al.* 1978; O'Nions, Evenson & Hamilton 1979; Ringwood 1979). The importance of the interpretation of seafloor flattening provided here, in the context of whole mantle convection, is that it provides independent corroboration of the assumptions of the thermal history calculations. The extent to which the interpretation is correct is a question which may be answered by further developments of numerical models of the mantle convective circulation. If this is correct and if the core contains no radioactivity then the planet is surely cooling.

References

Bénard, M. H., 1901. Les tourbillons cellulaires dans une nappe liquid transportant de la chaleur par convection en régime permanent, *Annls Chim. Phys.*, **XXIII**, 62–144.

Boussinesq, J., 1903. *Théorie Analytique de la Chaleur mise en Harmonie avec la Thermodynamique et avec la Théorie Mécanique de la Lumière*, Tome II, pp. 157–176, Gauthier-Villars, Paris.

Busse, F. H., 1981. On the aspect ratios of two-layer mantle convection, *Phys. Earth planet. Int.*, **24**, 320–324.

Cassen, P., Reynolds, R. T., Graziani, F., Summers, A., McNellis, J. & Blalock, L., 1979. Convection and lunar thermal history, *Phys. Earth planet. Int.*, **19**, 183–196.

Chandrasekhar, S., 1961. *Hydrodynamic and Hydromagnetic Stability*, Oxford, Clarendon Press, 652 pp.

Daly, S. F., 1978. Convection with decaying heat sources and the thermal evolution of the mantle, *PhD thesis*, University of Chicago, Chicago, Illinois, USA.

Daly, S. F., 1980. Convection with decaying heat sources: constant viscosity, *Geophys. J. R. astr. Soc.*, **61**, 519–547.

Davies, G. F., 1977. Whole-mantle convection and plate tectonics, *Geophys. J. R. astr. Soc.*, **49**, 459–486.

Davies, G. F., 1980. Thermal histories of convective Earth models and constraints on radiogenic heat production in the Earth, *J. geophys. Res.*, **85**, 2517.

De la Cruz, S., 1970. Asymmetric convection in the upper mantle, *Geofis. Int.*, **10**, 49–56.

De la Cruz, S., 1973. Convection with internal heat generation, *MSc thesis*, University of Toronto, Toronto, Ontario, Canada.

Elsasser, W. M., 1971. Two-layered model of upper-mantle convection, *J. Geophys. Res.*, **76**, 4744–4753.

Elsasser, W. M., Olson, P. & Marsh, B. D., 1979. The depth of mantle convection. *J. geophys. Res.*, **84**, 147–155; correction: **84**, 613.

Hess, H. H., 1962. History of ocean basins, in *Petrologic Studies: a Volume in Honor of A.F. Buddington*, pp. 599–620, eds Engel, A. E. J., James, H. L. & Leonard, B. F., Geological Society of America.

Hewitt, J. M., McKenzie, D. P. & Weiss, N. O., 1975. Dissipative heating in convective flows, *J. Fluid Mech.*, **68**, 721–738.

Hsui, A. T., Turcotte, D. L. & Torrance, K. E., 1972. Finite-amplitude thermal convection within a self-gravitating fluid sphere, *Geophys. Fluid Dyn.*, **3**, 35–44.

Jarvis, G. T. & McKenzie, D. P., 1980. Convection in a compressible fluid with infinite Prandtl number, *J. Fluid Mech.*, **96**, 515–583.

Jarvis, G. T. & Peltier, W. R., 1980. Oceanic bathymetry profiles flattened by radiogenic heating in a convecting mantle, *Nature*, **285**, 649–651.

Jeffreys, H., 1926. The stability of a layer of fluid heated below, *Phil. Mag. Series VII*, **2**, 833–844.

Jeffreys, H., 1930. The instability of a compressible fluid heated below, *Proc. Camb. phil. Soc.*, **26**, 170–172.

Kaula, W. M., 1979. Thermal evolution of Earth and Moon growing by planetesimal impacts, *J. geophys. Res.*, **84**, 999–1008.

Landau, L. D. & Lifshitz, E. M., 1959. *Fluid Mechanics*, Pergamon Press, Oxford, 536 pp.

Lux, R. A., Davies, G. F. & Thomas, J. H., 1979. Moving lithospheric plates and mantle convection, *Geophys. J. R. astr. Soc.*, **57**, 209–228.

Malkus, W. V. R., 1964. Boussinesq equations and convection energetics, *Geophys. Fluid Dyn.*, Woods Hole Oceanographic Institute, Ref. No. 64–46.

McKenzie, D. P., 1977. Surface deformation, gravity anomalies and convection, *Geophys. J. R. astr. Soc.*, **48**, 211–238.

McKenzie, D. P. & Richter, F. M., 1976. Convection currents in the Earth's mantle, *Sci. Am.*, **235**, 72–89.

McKenzie, D. P. & Weiss, N. O., 1975. Speculations on the thermal and tectonic history of the earth, *Geophys. J. R. astr. Soc.*, **42**, 131–174.

McKenzie, D. P., Roberts, J. M. & Weiss, N. O., 1974. Convection in the earth's mantle: towards a numerical simulation, *J. Fluid Mech.*, **62**, 465–538.

Mihaljan, J. M., 1962. A rigorous exposition of the Boussinesq approximations applicable to a thin layer of fluid, *Astrophys. J.*, **136**, 1126–1133.

Moore, D. R. & Weiss, N. O., 1973. Two-dimensional Rayleigh–Bénard convection, *J. Fluid Mech.*, **58**, 289–312.

O'Connell, R. J., 1977. On the scale of mantle convection, *Tectonophys.*, **38**, 119–136.

Olson, P. & Corcos, G. M., 1980. A boundary layer model for mantle convection with surface plates, *Geophys. J. R. astr. Soc.*, **62**, 195–219.

O'Nions, R. K., Evenson, N. M. & Hamilton, P. J., 1979. Geochemical modelling of mantle differentiation and crustal growth, *J. geophys. Res.*, **84**, 6091–6101.

O'Nions, R. K., Evenson, N. M., Hamilton, P. J. & Carter, S. R., 1978. Melting of the mantle past and present: isotope and trace element evidence, *Phil. Trans. R. Soc. A*, **288**, 547–559.

Oxburgh, E. R. & Turcotte, D. L., 1978. Mechanisms of continental drift, *Rep. Prog. Phys.*, **41**, 1249–1312.

Parmentier, E. M. & Turcotte, D. L., 1978. Two-dimensional mantle flow beneath a rigid accreting lithosphere, *Phys. Earth planet. Int.*, **17**, 281–289.

Parsons, B. & McKenzie, D. P., 1978. Mantle convection and the thermal structure of the plates, *J. geophys. Res.*, **83**, 4485–4496.

Parsons, B. & Sclater, J. 1977. An analysis of the variation of ocean floor bathymetry and heat flow with age, *J. geophys. Res.*, **82**, 803–827.

Peltier, W. R., 1972. Penetrative convection in the planetary mantle, *Geophys. Fluid Dyn.*, **5**, 47–88.

Peltier, W. R., 1980. Mantle convection and viscosity, in *Physics of the Earth's Interior*, Proc. Enrico Fermi International School of Physics, course LXXVIII, eds Dziewonski, A. & Boschi, E. North Holland, New York.

Peltier, W. R., 1981. Ice age geodynamics, *Ann. Rev. Earth planet. Sci.*, **9**, 199–225.

Peltier, W. R., Farrell, W. E. & Clark, J. A., 1978. Glacial isostasy and relative sea level: a global finite element model, *Tectonophys.*, **50**, 81–110.

Richter, F. M., 1973a. Dynamical models for sea floor spreading, *Rev. Geophys. Space Phys.*, **11**, 223–287.

Richter, F. M., 1973b. Convection and the large-scale circulation of the mantle, *J. geophys. Res.*, **78**, 8735–8745.

Richter, F. M. & McKenzie, D. P., 1978. Simple plate models of mantle convection, *J. Geophys.*, **44**, 441–471.

Richter, F. M. & McKenzie, D. P., 1981. Parameterizations for the horizontally averaged temperature of infinite Prandtl number convection, *J. geophys. Res.*, **86**, 1738–1744.

Richter, F. M. & Parsons, B., 1975. On the interaction of two scales of convection in the mantle, *J. geophys. Res.*, **80**, 2529–2541.

Ringwood, A. E., 1979. *Origin of the Earth and Moon*, Springer-Verlag, New York, 295 pp.

Roberts, G. O., 1977. Fast viscous convection, *Geophys. astrophys. Fluid Dyn.*, **8**, 197–233.

Roberts, G. O., 1979. Fast viscous Bénard convection, *Geophys. astrophys. Fluid Dyn.*, **12**, 235–272.

Roberts, P. H., 1967. Convection in horizontal layers with internal heat generation. Theory, *J. Fluid Mech.*, **30**, 33–49.

Schubert, G., Cassen, P. & Young, R. E., 1979. Subsolidus convective cooling histories of terrestrial planets, *Icarus*, **38**, 192–211.

Schubert, G., Yuen, D., Froidevaux, C., Fleitout, L. & Souriau, M., 1978. Mantle circulation with partial shallow return flow: effects on stresses in oceanic plates and topography of the sea floor, *J. geophys. Res.*, **83**, 745–758.

Sharpe, H. N. & Peltier, W. R., 1978. Parameterized mantle convection and the Earth's thermal history, *Geophys. Res. Lett.*, **5**, 737–740.

Sharpe, H. N. & Peltier, W. R., 1979. A thermal history model for the Earth with parameterized convection, *Geophys. J. R. astr. Soc.*, **59**, 171–205.

Spiegel, E. A. & Veronis, G., 1960. On the Boussinesq approximation for a compressible fluid, *Astrophys. J.*, **131**, 442–447.

Straus, J. M., 1972. Finite amplitude doubly diffusive convection, *J. Fluid Mech.*, **56**, 353–374.

Swarztrauber, P. N. & Sweet, R., 1975. Efficient FORTRAN subprograms for the solution of elliptic partial differential equations, *Rep. No. NCAR-TN/IA-109*, National Centre for Atmospheric Research, Boulder, Colorado.

Tozer, D. C., 1967. Towards a theory of thermal convection in the mantle, in *The Earth's Mantle*, pp. 325–353, ed. Gaskell, T. F., Academic Press, New York.

Tozer, D. C., 1972. The present thermal state of the terrestrial planets, *Phys. Earth planet. Int.*, **6**, 182–197.

Tozer, D. C., 1974. The internal evolution of planetary-sized objects, *Moon*, **9**, 167–182.

Tritton, D. J. & Zarraga, M. N., 1967. Convection in horizontal layers with internal heat generation. Experiments, *J. Fluid Mech.*, **30**, 21–31.

Turcotte, D. L., Cooke, F. A. & Willeman, R. J., 1979. Parameterized convection within the moon and the terrestrial planets, *Proc. Tenth Lunar and Planetary Science Conference*, Houston, Texas, March 19–23, *Volume 3: Planetary Interiors and Surfaces*, Pergamon Press, New York; *Suppl. Geochim. Cosmochim. Acta*, **11**, 2375–2392.

Turcotte, D. L. & Oxburgh, E. R., 1967. Finite amplitude convection cells and continential drift, *J. Fluid Mech.*, **28**, 29–42.

Turcotte, D. L. & Oxburgh, E. R., 1972. Mantle convection and the new global tectonics, *Ann. Rev. Fluid Mech.*, **4**, 33–68.

Weertman, J., 1970. The creep strength of the Earth's mantle, *Rev. Geophys. Space Phys.*, **8**, 145–168.

Young, R. E., 1974. Finite-amplitude thermal convection in a spherical shell, *J. Fluid Mech.*, **63**, 695–721.

Yuen, D. A., Tovish, A. & Schubert, G., 1978. Shear flow beneath oceanic plates: local nonsimilarity boundary layers for olivine rheology, *J. geophys. Res.*, **83**, 759–765.

Zebib, A., Schubert, G. & Straus, J., 1980. Infinite Prandtl number thermal convection in a spherical shell, *J. Fluid Mech.*, **97**, 257–277.